Atmospheric
Chemistry
and Physics

Open Access

Research article

Characterizing the near-global cloud vertical structures over land using high-resolution radiosonde measurements

Hui Xu[1], Jianping Guo[1], Bing Tong[2], Jinqiang Zhang[3], Tianmeng Chen[1], Xiaoran Guo[1], Jian Zhang[4], and Wenqing Chen[5]

[1]State Key Laboratory of Severe Weather, Chinese Academy of
Meteorological Sciences, Beijing, 100081, China
[2]State Key Laboratory of Urban and Regional Ecology, Research Center for Eco-environmental Sciences,
Chinese Academy of Sciences, Beijing, 100085, China
[3]Key Laboratory of Middle Atmosphere and Global Environment Observation, Institute of Atmospheric
Physics, Chinese Academy of Sciences, Beijing, 100029, China
[4]Hubei Subsurface Multi-Scale Imaging Key Laboratory, Institute of Geophysics and Geomatics,
China University of Geosciences, Wuhan, 430074, China
[5]Business Science and Technology Division, National Meteorological
Information Centre, Beijing, 100081, China

Correspondence: Jianping Guo (jpguocams@gmail.com) and Bing Tong (bingtong@rcees.ac.cn)

Abstract. Cloud remains one of the largest uncertainties in weather and climate research due to the lack of fine-resolution observations of cloud vertical structure (CVS) on a large scale. In this study, near-global CVS is characterized by high-vertical-resolution twice-daily radiosonde observations from 374 stations over land, which are distributed in Europe, North America, East Asia, Australia, the Pacific Ocean, and Antarctica. To this end, we initially develop a novel method to determine CVS, by combining both the vertical gradients of air temperature and relative humidity (RH) and the altitude-dependent thresholds of RH. It is found that the cloud base heights (CBHs) from radiosondes have a higher correlation coefficient ($R = 0.91$) with the CBHs from a millimeter-wave cloud radar than those from the ERA5 reanalysis ($R = 0.49$). Overall, cloudy skies occur 65.3 % (69.5 %) of the time, of which 55.4 % (53.8 %) are one-layer clouds at 00:00 (12:00) UTC. Most multi-layer clouds are two-layer clouds, accounting for 62.2 % (61.1 %) among multi-layer clouds at 00:00 (12:00) UTC. Geographically, one-layer clouds tend to occur over arid regions, whereas two-layer clouds do not show any clear spatial preference. The cloud bases and tops over arid regions are higher compared with humid regions albeit with smaller cloud thickness (CT). Clouds tend to have lower bases and thinner layer thicknesses as the number of cloud layer increases. The global-mean CT, CBH, and cloud top height (CTH) are 4.89 ± 1.36 (5.37 ± 1.58), 3.15 ± 1.15 (3.07 ± 1.06), and 8.04 ± 1.60 (8.44 ± 1.52) km above ground level (a.g.l.) at 00:00 (12:00) UTC, respectively. The occurrence frequency of clouds is bimodal, with lower peaks between 0.5 and 3 km a.g.l. and upper peaks between 6 and 10 km a.g.l. The CBH, CTH, and CT undergo almost the same seasonality; namely, their magnitudes in boreal summer are greater than in boreal winter. As expected, the occurrence frequencies of clouds exhibit pronounced diurnal cycles in different seasons. In boreal summer, clouds tend to form as the sun rises and the occurrence frequencies increase from morning to late afternoon, with the peak in the early afternoon at the altitude of 6–12 km a.g.l., while in boreal winter, clouds have peak occurrence frequencies in the morning. The relations between surface meteorological variables and moisture with CBH are investigated as well, showing that CBHs are generally more significantly correlated with 2 m relative humidity ($RH_{2\,m}$) and 2 m air temperature ($T_{2\,m}$) than with surface pressure and 10 m wind speed. Larger $T_{2\,m}$ and smaller $RH_{2\,m}$ always

correspond to higher CBH. In most cases CBHs are negatively correlated to soil water content. The near-global CVS obtained from high-vertical-resolution radiosondes in this study can provide key data support for improving the accuracy of cloud radiative forcing simulation in climate models.

1 Introduction

Clouds cover nearly two-thirds of Earth's surface area and have a significant impact on the radiative budget of the Earth–atmosphere system (e.g., Ramanathan et al., 1989; Houghton et al., 1996; Crewell et al., 2004; Stephens, 2005; Trenberth et al., 2009). Many studies have pointed out that the cloud radiative effects (CREs) are critically dependent on the height of clouds (e.g., Wielicki et al., 1995; Weare, 2000; Nam et al., 2012; Stephens et al., 2012; Wild, 2012; Lee et al., 2015; George et al., 2018). Different cloud types defined by cloud height can even cause two opposite CREs (i.e., the "greenhouse" and the "umbrella" effects; Meehl and Washington, 1995). Low and thick clouds tend to cool the surface through reflecting solar radiation, whereas high and thin cirrus clouds tend to warm the surface by preventing longwave radiation emitting outward (Liou, 1986; Naud et al., 2003; Solomon et al., 2007). Even small variations in cloud vertical structure (CVS) can lead to significant differences in the mean CRE and radiative heating/cooling rates (Costa-Surós et al., 2014). However, the vertical structures of clouds are often not accurately represented in current climate models, leading to large uncertainties in estimating the CRE (e.g., Randall et al., 2003; Waliser et al., 2009; Cesana and Chepfer, 2012; Cesana and Waliser, 2016; IPCC, 2021). Therefore, it is imperative to procure high-quality global CVS to improve the predictive capabilities of current climate models.

Satellite observations are efficient in detecting cloud properties. Passive satellite sensors like the Moderate Resolution Imaging Spectroradiometer (MODIS) can resolve a global coverage of cloud fraction and top height but not the vertical information of clouds (Platnick et al., 2003). Chang and Li (2005) retrieved near-global CVS for one-layer and overlapped clouds based on MODIS data. However, these retrievals lack the vertical structures of three- or multi-layer clouds. Active sensors such as the Cloud-Aerosol Lidar With Orthogonal Polarization (CALIOP) on board CALIPSO (Cloud-Aerosol Lidar and Infrared Pathfinder Satellite Observations; Winker et al., 2009) and the millimeter-wave cloud profiling radar (CPR) on board CloudSat (Stephens et al., 2002) can provide vertical structure of cloud layers on global scale (Oreopoulos et al., 2017). However, active sensors have relatively long revisit periods (e.g., 16 d) and narrow nadir views (e.g., Winker et al., 2007; Kim et al., 2011; Guo et al., 2016).

Ground-based instruments, such as lidars (Gouveia et al., 2017), ceilometers (Costa-Surós et al., 2013), and cloud radars (Mace et al., 1998), have proven to be effective in providing CVS with continuous temporal coverage and relatively high accuracy (Hahn et al., 2001; Zhou et al., 2020). Lidars and ceilometers can pinpoint cloud bases, and cloud radars can resolve multi-layer clouds (Willen et al., 2005; Nowak et al., 2008; Reddy et al., 2018). The US Department of Energy's Atmospheric Radiation Measurement Program (ARM) Climate Research Facility (http://www.arm. gov, last access: 20 July 2023) provides ground-based radar and lidar observations at fixed field sites, the North Slope of Alaska (NSA; Zhang et al., 2017), the Southern Great Plains (SGP; Dong et al., 2008), the tropical western Pacific (TWP; Comstock et al., 2013), and the eastern North Atlantic (ENA; Giangrande et al., 2019), and several mobile field sites (Cadeddu et al., 2013). These measurements provide information on the vertical structure of clouds (Stokes and Schwartz, 1994; Ackerman and Stokes, 2003) and have been widely used to study the cloud properties on global climate (Mace and Benson, 2008; Chandra et al., 2015). However, the global coverage of these instruments is too sparse and limited.

Radiosondes can provide reliable measurements of the profiles of air temperature (T) and relative humidity (RH) at a great many locations on a global scale (although underrepresented over oceans), making it possible to obtain global CVS given that the cloud formation is highly associated with the water vapor and thermal conditions of the atmosphere (e.g., Poore et al., 1995; Wang and Rossow, 1995; Chernykh and Eskridge, 1996; Wang et al., 2000; Minnis et al., 2005; Zhang et al., 2010). In order to detect CVS from radiosonde observations, two main methods have been proposed. One is the threshold method, in which cloud layers are determined using RH thresholds. Poore et al. (1995) proposed a T-dependent dewpoint depression threshold for cloud detection, and they found that only high clouds exhibited strong latitudinal and seasonal variation in the thickness of cloud layer. Wang and Rossow (1995) detected cloud layers using a single RH threshold, with the maximum and minimum RH thresholds of 87 % and 84 %, respectively. They demonstrated that the occurrence frequency of multi-layer clouds varied geographically, and multi-layer clouds occurred most frequently in the tropics. Zhang et al. (2010) improved the single threshold method using an altitude-dependent RH thresholds to characterize the base and top of cloud layers, and they demonstrated that multilayer clouds occurred more frequently in the summer. Another method is the gradient method, in which cloud layers are obtained by examining the variations of RH and T profiles. Chernykh and Eskridge (1996) used a second derivative of the vertical profiles of RH

and T to determine cloud boundaries, and they indicated that the accuracy of the prediction of cloud level is independent of the level type and location. Dzambo and Turner (2016) identified cirrus based on a cirrus cloud detection algorithm using radiosonde and cloud radar data and found that RH with respect to ice within cirrus clouds varied seasonally, with the maximum occurring in winter and the minimum in summer. To ensure the radiosonde measurements were collocated with the appropriate millimeter-wave cloud radar (MMCR) measurements, they established temporal ("lag time") and spatial restrictions. However, by comparing the CVS derived from above methods with ground-based remote-sensing measurements, Costa-Surós et al. (2014) indicated that the performances of these mentioned CVS retrieval methods may need further improvement. The possible reasons can be concluded as the following: (1) the vertical resolution of atmospheric profiles provided by radiosondes is low (e.g., 76 m; Poore et al., 1995), and (2) refined RH thresholds remain lacking for cloud detection.

With the emergence of a growing number of high-vertical-resolution (5–10 m) radiosonde measurements worldwide, improved retrievals of CVS on a large scale are now plausible. However, to our knowledge, no studies have reported near-global CVS from high-resolution radiosonde measurements. The main objective of the present study is to provide the first attempt to retrieve near-global vertical structures of clouds, including the number of cloud layers, cloud base height (CBH), cloud top height (CTH), and cloud thickness (CT) of each layer, using 2 years' worth (2018–2019) of high-vertical-resolution (5–10 m) radiosonde observations from 374 radiosonde stations across the world (e.g., Europe, North America, East Asia, Australia, the Pacific Ocean, and Antarctica). In order to obtain better CVS results, we first develop a novel CVS detection method that integrates the two main methods mentioned above by considering both the vertical gradients of RH and T, as well as the altitude-dependent thresholds of RH. The radiosonde-derived CVS is compared with that obtained by MMCR observations and ERA5 reanalysis. Unless otherwise noted, CBH represents the base for the lowermost cloud layer, CTH represents the top for the uppermost cloud layer, and CT represents the total cloud thickness (CTH − CBH). The remainder of this paper proceeds as follows: Sect. 2 describes the data and methods to determine the CVS. The performance of the CVS retrieved in this study is evaluated in Sect. 3. We analyze the frequency of clouds with various layers, their vertical and horizontal distributions, and the diurnal variation of cloud occurrence frequency with height. To examine the potential key factors that affect the CVS, we also investigate the relationship between CBH, surface meteorological variables, and moisture. The main conclusions are summarized in Sect. 4.

2 Data and methods

2.1 Data

2.1.1 High-resolution radiosonde data

Radiosonde instruments provide in situ measurements of atmospheric environmental variables, including RH, T, pressure, and wind profiles, which are recognized to be able to derive the vertical distribution of cloud (Chernykh and Eskridge, 1996). Radiosonde measurements are usually made twice a day at 00:00 and 12:00 UTC. For high-resolution radiosondes, the sampling period is approximately 1–2 s, and the vertical resolution is approximately 5–10 m throughout the atmosphere (Guo et al., 2016, 2019, 2021). In this study, high-vertical-resolution radiosonde measurements obtained from 426 sites across the globe are provided by several organizations, including the China Meteorological Administration (CMA), the National Oceanic and Atmospheric Administration (NOAA) of the United States, the Deutscher Wetterdienst (Climate Data Center) of Germany, the Centre for Environmental Data Analysis (CEDA) of the United Kingdom, the Global Climate Observing System (GCOS) Reference Upper Air Network (GRUAN), and the University of Wyoming. In total, there are more than 400 profiles at most radiosonde stations, which provide a roughly even distribution of near-global and sufficient samples to characterize the climatology of the CVS. To minimize the uncertainty in results, the radiosonde stations with the profile number less than 400 are not included, and radiosonde measurements at the remaining 374 stations are used to derive near-global CVS. The remaining 374 radiosonde stations include 120 L-band radiosonde stations from the CMA, 150 stations from NOAA, and 104 stations from the Deutscher Wetterdienst (Climate Data Center), the CEDA, the GRUAN, and the University of Wyoming. Overall, 407 688 soundings at near-global 374 high-vertical-resolution radiosonde stations for the period of 2018–2019 are used here, including 206 130 soundings at 00:00 UTC and 201 558 soundings at 12:00 UTC. The geographic distribution of the numbers of profiles at these radiosonde stations is displayed in Fig. 1.

The Vaisala RS92 radiosonde is widely used by NOAA, the Deutscher Wetterdienst, the CEDA, and the University of Wyoming. The Vaisala RS92 humidity sensor measures RH every 2 s (Wang et al., 2018), and its uncertainty is 5 % RH (Jauhiainen and Lehmuskero, 2005). Due to solar radiation heating, the RH data result in a dry bias in the upper troposphere (Vömel et al., 2007). Several correction algorithms have been developed to correct the solar radiation dry bias (e.g., Vömel et al., 2007; Cady-Pereira et al., 2008; Yoneyama et al., 2008; Miloshevich et al., 2009; Wang et al., 2013). The Vaisala RS41 radiosonde is used in the stations of GRUAN. Since temperature of the humidity sensor can be measured by the temperature sensor and taken into account in the RH calculation, no separate solar radiation dry-bias correction is needed for the RS41 humidity measure-
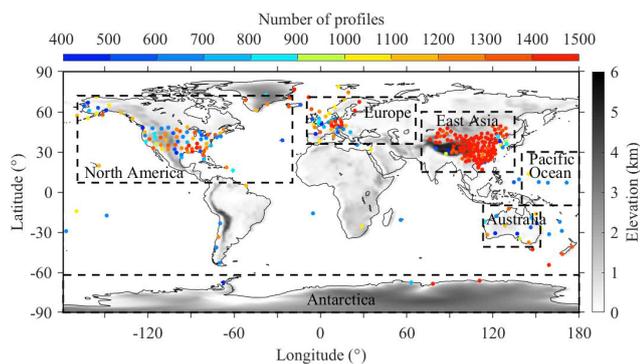
Figure 1. Geographic distribution of the number of profiles (colored full circle) for the near-global high-resolution radiosonde observation stations from 2018 to 2019. Also shown is the elevation of each radiosonde site in grey-scale shading. Black rectangles denote observation coverage in six regions of interest (i.e., Europe, North America, East Asia, Australia, the Pacific Ocean, and Antarctica). The numbers of radiosonde stations within Europe, North America, East Asia, Australia, the Pacific Ocean, and Antarctica are 44, 150, 120, 13, 5, and 4, respectively. The numbers of radiosonde stations in the Northern Hemisphere (NH) and Southern Hemisphere (SH) are 338 and 36, respectively.

ment (Jensen et al., 2016). The RS41 humidity sensor has an uncertainty of 3 % RH (Vaisala, 2017). The GTS1 digital radiosonde is used by CMA, having the advantages of high sensitivity, quick sampling, and small volume (Li, 2006; Bian et al., 2011; Chen et al., 2021). The humidity sensor of GTS1 samples RH at a time interval of approximately 1 s, with an uncertainty of about 5 % RH (Li et al., 2009). The specifications for the Vaisala RS92, Vaisala RS41, and GTS1 digital radiosonde are shown in Table 1.

2.1.2 Ka-band millimeter-wave cloud radar

The Ka-band (35 GHz) MMCR (Moran et al., 1998) has the advantage of penetrating clouds and continuously detecting the vertical structure of clouds, which can reach an accuracy of 150 m for cloud boundaries (Clothiaux et al., 2000; Hollars et al., 2004). The CVSs extracted from MMCR are widely used as reference for inter-comparison with radiosonde-derived CVS (e.g., Naud et al., 2005; Zhang and Klein, 2013). In this study, we use the data measured by a Ka-band MMCR installed at Beijing Nanjiao weather observatory (BNWO; 39.81° N, 116.47° E; 32 m a.s.l.) from the Meteorological Observation Center of the CMA during the period of 2019. This MMCR can measure an altitude of 15 km a.g.l. with a vertical resolution of 30 m and a temporal resolution of 1 min. The CBHs and CTHs are identified based on the minimum threshold method using the MMCR reflectivity measurements (Zhang et al., 2019).

2.1.3 ERA5 reanalysis

The ERA5 is the fifth generation of global atmospheric, land, and oceanic climate reanalysis produced by the European Centre for Medium-Range Weather Forecasts (Bell et al., 2021). The ERA5 reanalysis dataset, covering 1979 to present, is produced using 4D-Var data assimilation and is closely associated with the excellence of the forecast products. The temporal and spatial resolutions of ERA5 can reach up to 1 h and $0.25° \times 0.25°$, respectively (Hersbach et al., 2020). The product consists of single-level variables (e.g., CBH and total cloud fraction) on one level or near-surface, pressure-level variables (e.g., temperature and relative humidity) on 37 levels from 1000 to 1 hPa, and model-level variables on 137 levels from the surface to a height of 80 km a.s.l. (https://cds.climate.copernicus.eu/cdsapp#!/dataset/reanalysis-era5-complete?tab=overview, last access: 10 October 2023). As a key variable that links land surface to cloud formation, soil moisture from the ERA5 reanalysis has been widely used in the analysis of land–atmosphere coupling (Sun et al., 2020). Using the ERA5 reanalysis in East Asia, Wei et al. (2021) explored the relationships between soil moisture, land surface sensible and latent heat fluxes, and CBH and found negative correlations between soil moisture and CBH. In this study, we use five meteorological variables such as the 10 m u component of wind (u), 10 m v component of wind (v), surface pressure (PS), 2 m air temperature ($T_{2\,m}$), and 2 m dewpoint temperature ($TD_{2\,m}$); two moisture variables (soil volumetric water content of the 0–7 cm layer (θ), and mean vertically integrated moisture flux divergence (MFD)); and two cloud variables, including total cloud fraction and CBH, both of which are obtained from the hourly single-level ERA5 reanalysis. In order to obtain the 2 m relative humidity ($RH_{2\,m}$), the equation proposed by Lawrence (2005) is used, which is shown as follows:

$$RH_{2\,m} = 100 - 5 \times (T_{2\,m} - TD_{2\,m}). \tag{1}$$

2.2 Methods

2.2.1 Pre-processing

Previous studies suggested that pure ice exists in part of the cloud when T drops below $-20\,°C$ (Minnis et al., 2005). Since radiosonde measurements only provide the RH profile with respect to liquid ($RH_{liquid}(z)$), the portion of radiosonde-observed $RH_{liquid}(z)$ should be converted to the RH profile with respect to ice ($RH_{ice}(z)$) for those observations at altitudes with T below $-20\,°C$ (Austin et al., 2009). According to Murray (1967) and Monteith and Unsworth (2008), $RH_{ice}(z)$ is converted from $RH_{liquid}(z)$ when $T < -20\,°C$ based on the following equations:

Table 1. The specifications of the Vaisala RS92, Vaisala RS41, and GST1 digital radiosonde.

Radiosonde characteristics	Vaisala RS92	Vaisala RS41	GTS1 digital radiosonde
Manufacturer	Vaisala Oyj, Finland	Vaisala Oyj, Finland	Shanghai Changwang Meteorological Science and Technology Company, China
Service period	2003 to present	2013 to present	2002 to present
Humidity sensor	Thin-film capacitor, heated twin HUMICAPS	Thin-film capacitor, integrated temperature sensor and heating functionality	Carbon-film hygristor
RH range	0 % to 100 %	0 % to 100 %	0 % to 100 %
RH uncertainty	5 % RH	3 % RH	∼ 5 % RH
Dry-bias corrections	Empirical mean bias correction algorithm (Miloshevich et al., 2009); NCAR radiation bias correction algorithm (Wang et al., 2013)	No separate solar radiation correction is needed	Humidity error correction based on fluid dynamic (Mao et al., 2016); PSO-BP neural network correction (Shan et al., 2018)
Vertical resolution	2 s	2 s	1 s
References	Jauhiainen and Lehmuskero (2005); Vömel et al. (2007); Miloshevich et al. (2009); Wang et al. (2013)	Jensen et al. (2016); Vaisala (2017)	Li (2006); Li et al. (2009); Bian et al. (2011); Chen et al. (2021)

$$e_{\text{liquid}}(z) = 6.1078 \exp\left[\frac{17.2693882\,T(z)}{T(z) + 237.3}\right], \quad (2)$$

$$e_{\text{ice}}(z) = 6.1078 \exp\left[\frac{21.8745584\,(T(z) - 3)}{T(z) + 265.5}\right], \quad (3)$$

$$\text{RH}_{\text{ice}}(z) = \text{RH}_{\text{liquid}}(z) \times \frac{e_{\text{liquid}}(z)}{e_{\text{ice}}(z)}, \quad (4)$$

where z represents altitude (in km); $T(z)$ represents the profile of air temperature (in °C); and $e_{\text{liquid}}(z)$ (hPa) and $e_{\text{ice}}(z)$ (hPa) denote saturation vapor pressure in the pure liquid and ice phase with respect to altitude, respectively. Note that the altitude represents the height above ground level (a.g.l.).

Note that besides Eq. (3), there are also several formulations for e_{ice} (Murphy and Koop, 2005). In order to quantify the difference in e_{ice}, we also calculate the e_{ice} for −40 to 0 °C using several equations listed in Murphy and Koop (2005), which are by Goff and Gratch (1946), Hyland and Wexler (1983), Sonntag (1990), and Marti and Mauersberger (1993). Obviously, the e_{ice} values calculated using different formulations are nearly the same (Fig. S1). Specifically, e_{ice} calculated by Murray (1967) is mostly close to that by Goff and Gratch (1946), with the absolute difference less than 0.004 hPa, followed by Hyland and Wexler (1983) and Sonntag (1990), with the absolute difference less than 0.009 hPa. The largest differences in e_{ice} exist between Murray (1967) and Marti and Mauersberger (1993), reaching up

to 0.012 hPa. These results could prove that our choice for e_{ice} calculation is expected to affect the CVS results slightly.

When T is between −20 and 0 °C, liquid water and ice coexist in cloud (Austin et al., 2009). In this case, the RH is termed RH_{mixed}, which is a combination of $\text{RH}_{\text{liquid}}$ and RH_{ice}. To obtain the RH_{mixed} profile, the solutions of ice phase and liquid phase are scaled linearly with $T(z)$ (Austin et al., 2009). Therefore, RH_{mixed} at any given height z can be calculated using the following equations:

$$\text{RH}_{\text{mixed}}(z) = \frac{-20 - T(z)}{-20}\text{RH}_{\text{liquid}}(z) + \frac{T(z)}{-20}\text{RH}_{\text{ice}}(z). \quad (5)$$

In our retrieval method, the final RH profile $\text{RH}(z)$ used to derive the CVS can be described as $\text{RH}_{\text{liquid}}(z)$, $\text{RH}_{\text{ice}}(z)$, and $\text{RH}_{\text{mixed}}(z)$, depending on the phase state, which are calculated using the following formula:

$$\text{RH}(z) = \begin{cases} \text{RH}_{\text{liquid}}(z), & T(z) \geqslant 0\,°\text{C} \\ \text{RH}_{\text{mixed}}(z), & -20\,°\text{C} < T(z) < 0\,°\text{C} \\ \text{RH}_{\text{ice}}(z), & T(z) \leqslant -20\,°\text{C}. \end{cases} \quad (6)$$

Before determination of CVS, the profiles of $\text{RH}(z)$ and $T(z)$ after the above pre-processing are smoothed by the arithmetical averages of $\text{RH}(z)$ and $T(z)$ at the altitudes of z_{i-1}, z, and z_{i+1} ($i \geq 2$), respectively.

2.2.2 Determination of CVS

The presence of clouds greatly affects the $\text{RH}(z)$ and $T(z)$, which changes sharply when a sounding balloon enters

or leaves cloud layers (Pietrowicz and Schiermeir, 1978; Matveev, 1981; Lawson and Cooper, 1990). Thus, the changes in the vertical gradients of $RH(z)$ and $T(z)$ can be used to identify cloud boundaries. Chernykh and Eskridge (1996) presented a method to determine cloud boundaries using the second derivatives of $RH(z)$ and $T(z)$ ($RH''(z)$ and $T''(z)$), respectively. However, only using $RH''(z)$ and $T''(z)$ would cause us to misidentify cloud layers, tending to detect more cloud layers than observations, especially for very thin cloud layers (Zhang et al., 2012; Costa-Surós et al., 2014). To reduce this possibility, the RH threshold should be combined to determine cloud layers. Zhang et al. (2010) proposed altitude-dependent thresholds of RH to detect cloud layers. However, their method tends to identify fewer cloud layers (Costa-Surós et al., 2014). This is due to the application of slightly high RH thresholds, resulting in a lower detection rate of clouds.

In order to improve the accuracy of cloud detection, we develop a CVS retrieval method by combining the vertical gradients of $RH(z)$ and $T(z)$ and altitude-dependent thresholds of RH as well. After pre-processing the $RH(z)$, the first step in our method is to detect the bases and tops of the moist layers. Generally, $RH(z)$ increases when a radiosonde balloon enters a moist layer, which suggests that the first derivative of $RH(z)$ is greater than zero ($RH'(z) > 0$). At the base of a moist layer, there is a jump in $RH(z)$ (Wang and Rossow, 1995), thus considering that $RH(z)$ reaches a local maximum increase ($RH''(z) < 0$). At the same time, $T(z)$ stops decreasing (i.e., $T'(z) < 0$) near the base of a moist layer, due to the condensation of water vapor and its accompanying release of latent heat. Hence, $T(z)$ reaches a local minimum decrease, which means $T''(z) > 0$. Therefore, by examining the first and second derivatives of $RH(z)$ and $T(z)$ starting from the surface upward, the bases of the moist layers can be detected when the following criteria are satisfied:

$$\begin{cases} RH'(z) > 0 \text{ and } RH''(z) < 0 \\ T'(z) < 0 \text{ and } T''(z) > 0, \end{cases} \tag{7}$$

where $RH'(z)$ and $RH''(z)$ denote the first and second derivatives of $RH(z)$, respectively, and $T'(z)$ and $T''(z)$ denote the first and second derivatives of $T(z)$, respectively.

Similarly, the tops of the moist layers are detected as follows:

$$\begin{cases} RH'(z) < 0 \text{ and } RH''(z) < 0 \\ T'(z) > 0 \text{ and } T''(z) > 0. \end{cases} \tag{8}$$

To obtain $RH''(z)$ and $T''(z)$, Chernykh and Eskridge (1996) approximated radiosonde-observed $RH(z)$ and $T(z)$ by cubic splines (Bartels et al., 1995), which led to bias in cloud detection. To avoid bias due to this approximation, we calculate

Table 2. Summary of altitude-dependent thresholds of RH.

Altitude range	Height-resolving RH thresholds		
	Min-RH	Max-RH	Inter-RH
0–2 km	84 %	94 %	82 %
2–6 km	80 %	92 %	78 %
6–12 km	78 %	88 %	70 %
> 12 km	70 %	80 %	70 %

$RH''(z)$ and $T''(z)$ as follows:

$$\begin{cases} RH'(z) = \frac{dRH(z)}{dz} = \frac{RH(z_{i+1}) - RH(z_i)}{z_{i+1} - z_i} \\ RH''(z) = \frac{d}{dz}(\frac{dRH}{dz}) = \frac{RH'(z_{i+1}) - RH'(z_i)}{z_{i+1} - z_i} \\ T'(z) = \frac{dT}{dz} = \frac{T(z_{i+1}) - T(z_i)}{z_{i+1} - z_i} \\ T''(z) = \frac{d}{dz}(\frac{dT}{dz}) = \frac{T'(z_{i+1}) - T'(z_i)}{z_{i+1} - z_i}. \end{cases} \tag{9}$$

Then, we identify cloud layers from moist layers determined above using height-resolving RH thresholds defined in Table 2, which are lower than the thresholds proposed by Zhang et al. (2010) to reduce the restriction for a moist layer being identified as a cloud layer. The moist layer is identified as a cloud layer if the following three conditions are met: (1) the base of the moist layer is greater than 280 m (Zhang et al., 2010); (2) the thickness of the moist layer is larger than 30.5 m and 61 m for the base of the moist layer less than 2 km and larger than 2 km, respectively (Poore et al., 1995; Zhang et al., 2010); (3) the minimum RH (min-RH) within the moist layer is greater than the corresponding min-RH threshold at the base of the moist layer (Table 2); and (4) the maximum RH (max-RH) within the moist layer is greater than the corresponding max-RH threshold at the base of the moist layer (Table 2). Using max-RH, it is possible to avoid misidentifying some thin moist layers as cloud layers. Otherwise, the moist layer is discarded from the analysis.

2.2.3 Post-processing

To obtain robust cloud structures, the cloud layers determined above have to be further reprocessed. If the distance between two contiguous cloud layers is less than 300 m, or the min-RH between the continues cloud layers is greater than the corresponding minimum RH threshold (inter-RH) between the consecutive cloud layers (Table 2), these two cloud layers are merged (Zhang et al., 2010).

The whole process, including the pre-processing of the RH profile, the determination of the cloud layers in vertical direction, and the post-processing of detected cloud layers, is schematically summarized in Fig. 2.

3 Results and discussion

3.1 Intercomparison of CVS from radiosondes, MMCR, and ERA5

Before presenting the characteristics of near-global vertical structure of clouds, we first compare the CVSs determined from radiosonde measurements using our proposed retrieval method with those from the MMCR in Beijing. Figure 3 presents the comparisons of the cloud base and top heights of each layer for four selected cases. As seen from Fig. 3a, the one-layer cloud derived from radiosondes (left) agrees well with that obtained by MMCR (right), with the CBH (CTH) being 0.28 (9.57) km and 0.48 (9.66) km for radiosondes and MMCR, respectively. For the high cloud case, the radiosonde-derived CBH and CTH are also consistent with those from MMCR (Fig. 3b). The radiosonde classifications of two-layer clouds are also in good agreement with those from MMCR (Fig. 3c and d). The above results indicate that radiosondes have the potential to obtain accurate CVS for both low cloud and high cloud, assuming that there is no obvious change in CVS during short time ($\sim$ 15 min).

For the statistical analysis during the whole year of 2019 in Beijing (Fig. 4), the cloud base and top heights obtained by radiosondes are generally consistent with those from MMCR, with correlation coefficients (R) being up to 0.91 and 0.81, respectively. Note that to collocate radiosonde-derived CBHs (CTHs) with appropriate MMCR-measured CBHs (CTHs), the time lag correction proposed by Dzambo and Turner (2016) is used. For low-level clouds (CBH < 2 km), the radiosonde-derived CBHs are obviously higher than those from MMCR. A possible reason is that MMCR detects cloud particles using the millimeter wavelength and is readily affected by the presence of large precipitation particles, as well as insects and bits of vegetation which are commonly suspended in the atmospheric boundary layer, resulting in a lower cloud base (Zhang et al., 2013). For CTHs, the values retrieved from radiosondes are systematically higher than those from MMCR by about 0.86 km (Fig. 4b). There are three possible reasons for this difference. One is related to the variations in clouds from radiosonde observations caused by the horizontal drift of radiosonde balloons (Clothiaux et al., 2000; Zhang et al., 2013), which may explain the large discrepancies. Another reason is that MMCR is not sensitive to small cloud particles far from the radar, thereby tending to underestimate CTH (Zhang et al., 2019). The last one is that radiosondes tend to detect higher cloud top heights than those retrieved from MMCR due to delay (time lag) after the radiosonde balloon passes through a cloud layer because of the wetness of the sensors (Zhang et al., 2013). Overall, the results of Figs. 3 and 4 indicate that our proposed CVS retrieval method is reliable and can detect CVS accurately and reasonably.

Next, we compare the radiosonde-derived CVS over 2018–2019 with those from ERA5 reanalysis on a global scale, as shown in Fig. 5. In general, the CBHs from ERA5 tend to be lower than those from radiosondes, and their R values are 0.24 and 0.49 at 00:00 UTC (Fig. 5a) and 12:00 UTC (Fig. 5b) for the whole data, respectively. This result is similar to that reported by Li et al. (2022), which demonstrated that the differences in CBHs between ERA5 and the surface observation are much higher at 00:00 UTC. The reason for that the correlation coefficient at 12:00 UTC is more than twice as large as at 00:00 UTC is complicated, which may be associated with the uncertainties of RH and T profiles, and the assimilation windows (within 12 h) for model constraint when producing hourly ERA5 data (Hersbach et al., 2020). At a more detailed level, the CBHs from ERA5 tend to be much lower than those from radiosondes for clouds with CBHs from radiosondes > 6 km. Previous studies reported that the underestimation for high-level clouds in the ERA5 results were caused by the poor specification or parameterization of critical RH from model (Miao et al., 2019). To clearly examine the case where most data exist in Fig. 5a and b, the comparison for CBHs from radiosondes < 2 km is further given at Fig. 5c and d. Compared to the results of all the cloud layers, the fitting slopes of the low cloud layers are slightly smaller, and the R values are smaller by about 25 %. This indicates that the CBHs from ERA5 are roughly underestimated compared with radiosonde observations at relatively low altitude. The reason may be associated with issues of cloud parameterizations schemes used for ERA5. The CBH in ERA5 is detected using the cloud cover or cloud water mixing ratio threshold. When cloud cover is greater than 1 %, the height from the ground is defined as CBH (Wang et al., 2022), which may lead to the underestimation of CBH in ERA5. Note that there are several cases with very low CBH from ERA5 (e.g., CBH < 0.1 km), which is not reasonable.

3.2 Statistic analysis of cloud occurrence frequency

The annual and seasonal frequency distributions of clouds with the number of layers at 12:00 UTC over 2018–2019 are presented in Fig. 6. On the annual timescale, a total of 201 558 profiles from radiosondes are retrieved. Of all detected profiles, 30.5 % cases are clear skies, indicating 69.5 % of the time is cloudy (Fig. 6a), which is in good agreement with the global-mean cloud fraction (about 68.0 % $\pm$ 3.0 %) reported by Stubenrauch et al. (2013), who analyzed the global cloud fraction using multiple satellite observations (e.g., MODIS, MISR, POLDER, and CALIPSO). Over cloudy skies, the cloud frequency decreases as the number of layers increases (Fig. 6a), with the one-, two-, three-, four-, five-, six-, and seven-layer clouds accounting for 53.8 %, 28.0 %, 11.4 %, 4.2 %, 1.4 %, 0.6 %, and 0.4 %, respectively. Wang et al. (2000) and Subrahmanyam and Kumar (2017) found similar decreasing trends using global radiosonde measurements (vertical resolution of $\sim$ 100 m) and global satellite observations (CALIOP), and they demonstrated that 58 % of clouds were one-layer clouds. However,
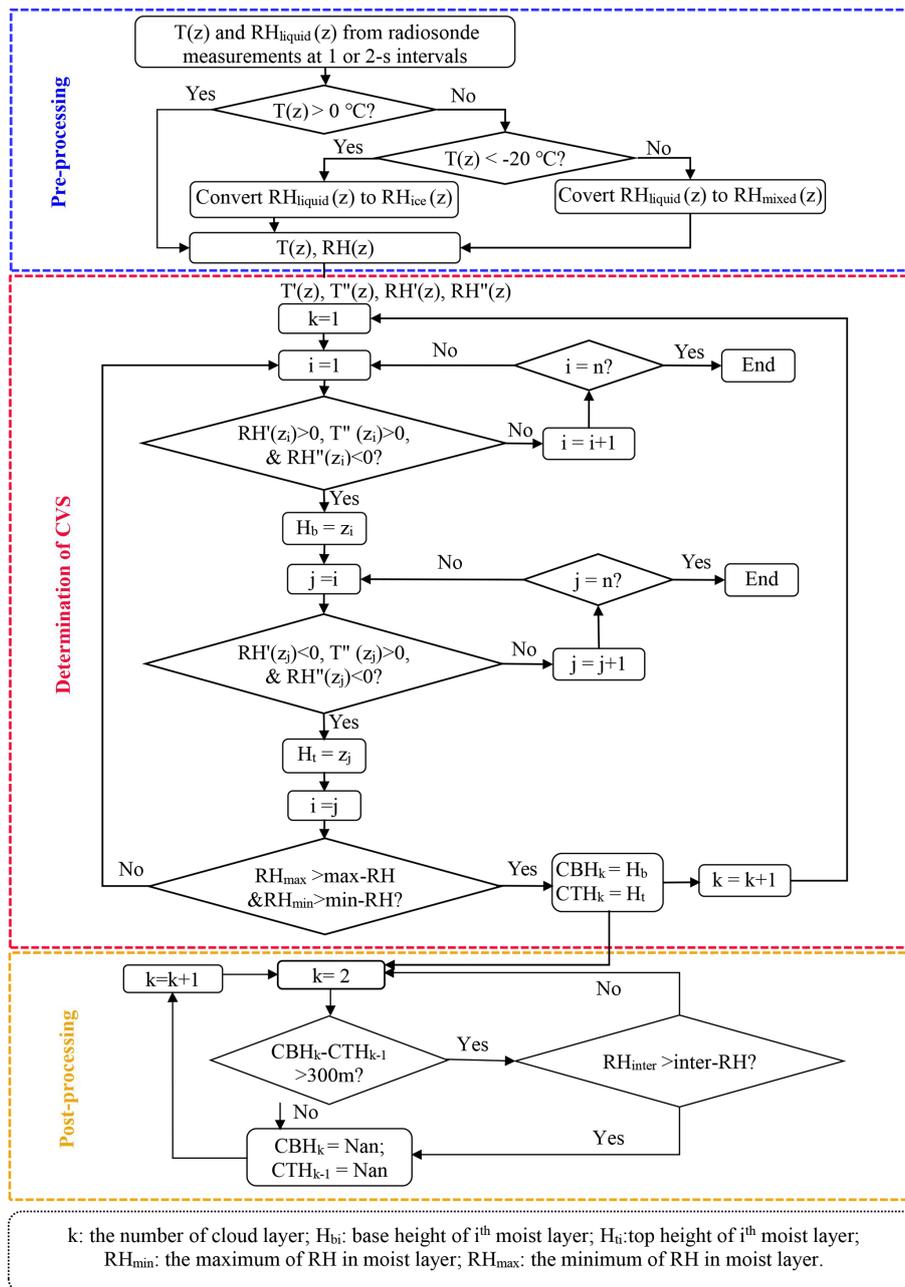
Figure 2. Flow chart showing the determination of the cloud vertical structure (CVS) using vertical profiles of air temperature (T) and relatively humidity (RH) from high-resolution radiosonde data and the altitude-dependent thresholds of RH defined in Table 2.

the occurrence frequencies of multi-layer clouds in our study are obviously higher than those provided by Subrahmanyam and Kumar (2017), which reported that two-, three-, four-, and five-layer clouds occurred at frequencies of 20.00 %, 3.50 %, 0.40 %, and 0.04 %, respectively. The possible cause for this difference could be that satellites have insufficient detection capabilities for multi-layer clouds, leading to an underestimation of their occurrence frequencies (Chang and Li, 2005).

Among the multi-layer clouds, 61.1 % are two-layer clouds. This result is slightly lower than that reported by Wang et al. (2000), who suggested that about 67 % of the multi-layer clouds were two-layer clouds. The possible reasons are the discrepancies in the study periods, the spatial distributions of radiosonde stations, the vertical resolution of the radiosonde measurements, and the CVS derivation methods. At 00:00 UTC, cloudy skies occur 65.3 % of the time. Of all cloud figuration, the occurrence frequency of one-layer
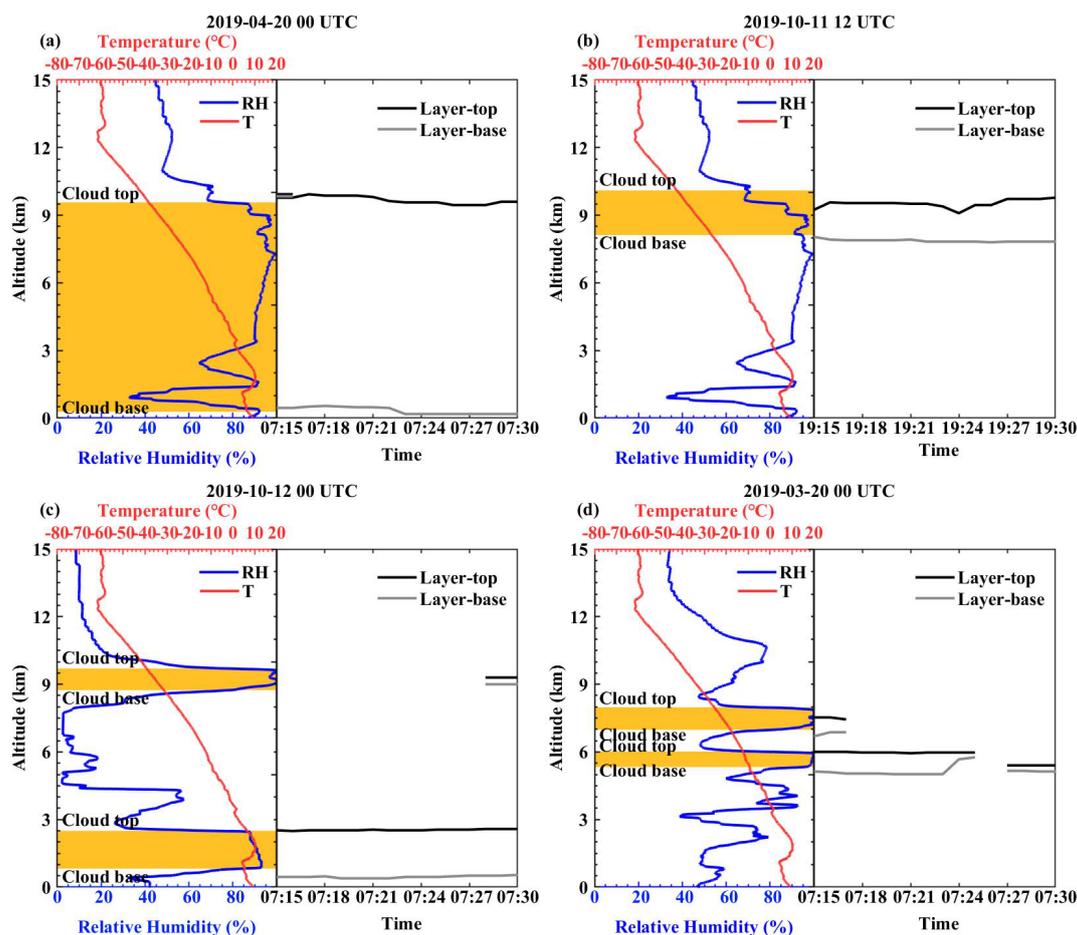
Figure 3. Examples of the detection of CVS by (left) high-resolution radiosondes and (right) Ka-band millimeter-wave cloud radar (MMCR) at the Beijing site for the four selected cases for **(a, b)** one-layer clouds and **(c, d)** two-layer clouds. Yellow shading represents the cloud layers retrieved from radiosondes. In each subfigure (left), the solid blue and red lines represent the RH and T profile, respectively.
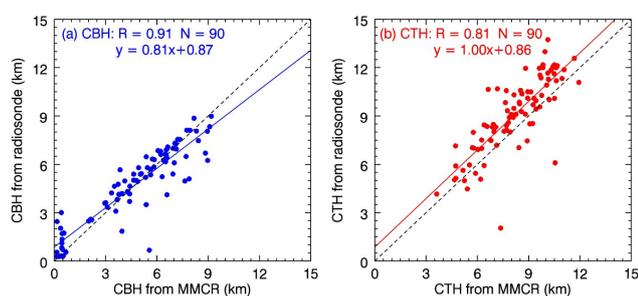
Figure 4. Scatter plots of the radiosonde-derived **(a)** cloud base heights (CBH) and **(b)** cloud top heights (CTH) versus those from the MMCR at the Beijing site during the year of 2019. R represents the correlation coefficient, and N represents the sample number. The dashed line and solid line in each panel denote the 1 : 1 line and the linear regression line, respectively.

clouds accounts for 55.4 %. Among multi-layer clouds detected, 62.2 % are two-layer clouds (Fig. S2a).

The seasonal frequency distributions of clouds with the number of layers (Fig. 6b, c, d, and e) are similar to those at the annual timescale; namely, their frequency decreases as the number of layers increases. By comparison, more clouds occur in December–January–February (DJF; 72 %) and March–April–May (MAM; 70.8 %) than they do in June–July–August (JJA; 69.3 %) and September–October–November (SON; 66.3 %). These results are consistent with those from Xi et al. (2010) based on a 10-year climatology of cloud fraction from surface observations. The seasonal variations are caused by the fact that cloud fractions vary monthly, with a maximum of 83 % in February and a minimum of 65 % in September (Fig. S3b). For one-layer clouds, the occurrence frequency is highest in MAM and DJF and lowest in JJA. The possible reason is that the radiosonde sites in this study are mainly located in the Northern Hemisphere (NH) (Fig. 1), and more stratus clouds occur in boreal winter (DJF) and boreal spring (MAM) than boreal summer (JJA) (Dong et al., 2005). In contrast, the occurrence frequency of multi-layer clouds is highest in boreal summer (JJA), owing to the
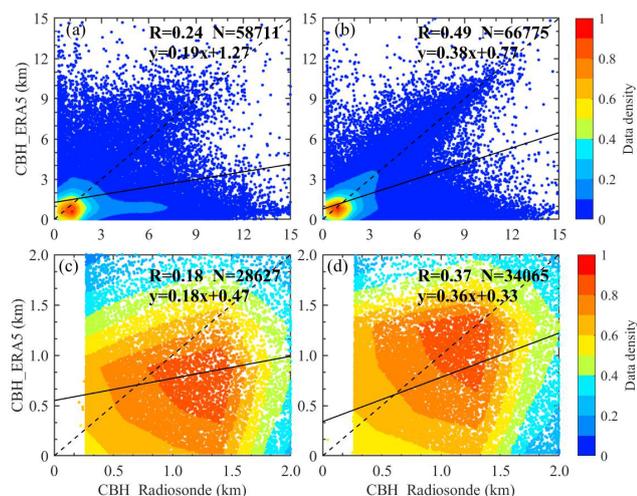
Figure 5. Scatter plots of the comparisons of the radiosonde-derived CBHs with those from ERA5 for all the data at **(a)** 00:00 and **(b)** 12:00 UTC and for the cases that both CBHs are less than 2.0 km at **(c)** 00:00 and **(d)** 12:00 UTC during the period of 2018–2019. Each point represents one measurement at 00:00 or 12:00 UTC. R represents the correlation coefficient, and N represents the sample number. The linear regression equation is also given, and the regression line is marked by a solid black line. The dashed black line is the 1 : 1 line.

deeper troposphere and more convective storms in summer (Zhang et al., 2010). The frequencies of clouds with various layers at 00:00 UTC on a seasonal scale (Fig. S2b, c, d, and e) are also similar to those at 12:00 UTC to some degree.

3.3   Near-global vertical distribution of cloud

The annual-mean CVSs for one-, two-, three-, four-, and five-layer clouds at 12:00 UTC are shown in Fig. 7a. In general, the CBH (CTH) decreases slightly (increases significantly) as the number of cloud layers increases. The CBHs of one-, two-, three-, four-, and five-layer cloud are 3.58 ± 3.31, 2.61 ± 2.76, 2.07 ± 2.44, 1.92 ± 2.49, and 1.97 ± 2.71 km, and the corresponding CTHs are 6.52 ± 3.94, 9.42 ± 3.04, 10.71 ± 2.94, 11.81 ± 3.04, and 13.17 ± 3.06 km, respectively. This result is consistent with Zhang et al. (2010), who reported that one-layer clouds are roughly located at altitudes that fall somewhere among the altitudes of the multi-layer cloud configurations. It is obvious that the lowermost cloud layer in multi-layer clouds occurs below 3 km with slight variations, while the upper layer exhibits more significant variations. Similarly, Wang et al. (2000) pointed out that the lowermost layers of two- and three-layer clouds occur mostly below 3 km, and the uppermost layer of two- and three-layer clouds occurs over a wide range of heights centered in 6 to 7 km and 7 to 8 km, respectively. Interestingly, the thickness of one-layer clouds (2.94 ± 3.00 km) is greater than that of multi-layer clouds of any number of layers (0.67 ± 0.88–2.44 ± 2.07 km), and the thickness of each cloud layer for

multi-layer clouds decreases as the number of cloud layers increases, which is consistent with previous studies (e.g., Luo et al., 2009; Chi et al., 2022). For multi-layer clouds, the thickness of the lowermost layer is larger than that of the upper layer. These CVS results are mainly attributed to the combined effects of solar heating and exchange of longwave radiation between surface and cloud layers (e.g., Rogers and Koracin, 1992; Guan et al., 1997; Zhang et al., 2010). Note that for the three-, four-, and five-layer cloud configurations, the maximum distance between two continues cloud layers is around 2.5 km, existing between the first and second lowest layer. For the upper layers, the distance between two continuous cloud layers decreases to be about 1.0 km.

To further quantify the CVS for one- and multi-layer clouds, their box plots are shown in Fig. 7b. Overall, for multi-layer clouds, the mean CBH is lower than that for the one-layer clouds by 1.20 km, while the mean CTH (CT) is much greater than that for one-layer by 3.47 km (4.67 km). The possible reasons are that multi-layer clouds often occur in humid climate regions (e.g., southeast of China and east of the United States as shown in Fig. 12c, d, e, and f), and the air parcel tends to reach the lift condensation level (LCL) at relatively low altitude, resulting in lower CBH compared to one-layer clouds. Most multi-layer clouds are generated from one-layer clouds by extending the range of CBH and CTH of one-layer clouds. Thus, we expect that the CTH and CT of multi-layer clouds are larger than those of one-layer clouds. Note that the different-layer cloud configurations occur at different frequencies as shown in Fig. 5a.

The CTH and CBH are two of the most important CVS parameters that play a significant role in estimating CRE at the top of the atmosphere and the surface, respectively (Wang and Rossow, 1995; Loeb et al., 2012; Xu et al., 2021b). In this study, we present the vertical distributions of annual and seasonal occurrence frequencies of CBH, CTH, and cloud at 12:00 UTC in Fig. 8. As references for altitude, the annual- and seasonal-mean planetary boundary layer height (PBLH) and tropopause height retrieved from radiosonde observations are also given in Fig. 8. Generally, these results of the vertical occurrence frequencies of clouds at an annual scale are close to those at a seasonal scale. It is obvious that the relatively large occurrence frequencies of CBH occur within 1 km, with the highest frequency being at about 0.5 km (Fig. 8a and d), which is lower than the annual-mean PBLH (~ 0.76 km). This indicates that most cloud bases exist in the atmospheric boundary layer, as shown in previous studies (Zhang et al., 2014). Above the top of the boundary layer, the occurrence frequencies of CBH decrease with altitude, since most clouds are suppressed by the inverse layer at the top of the boundary layer (Sugimoto et al., 2000). Over 6 km, the occurrence frequency of CBH in boreal summer (JJA) is higher than that in other seasons (Fig. 8d). The reason may partly be that more cirrus clouds occur in summer (Wang et al., 2000). Below 1.5 km, the occurrence frequency of CBH is the highest during boreal winter (DJF). This phe-
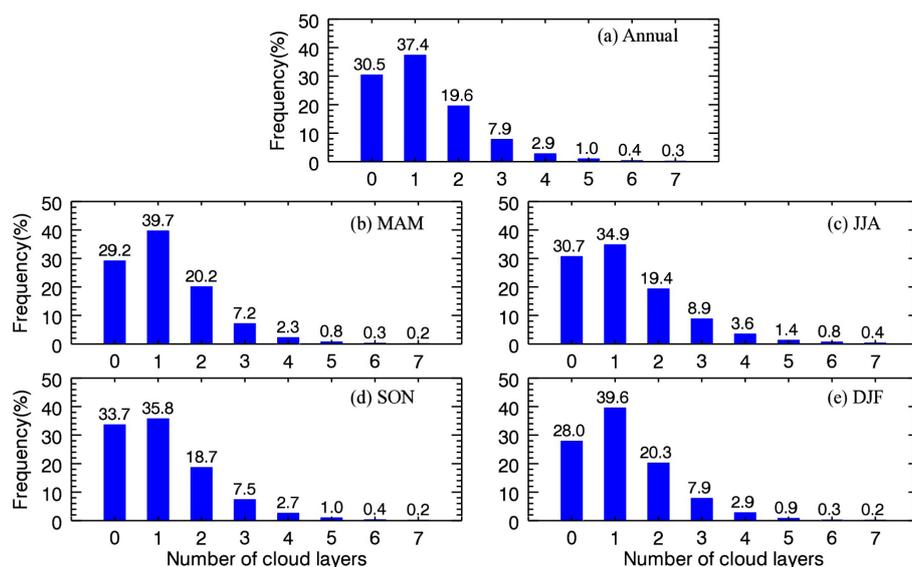
Figure 6. Near-global-mean occurrence frequencies of clouds with a variety of number of layers ranging from 0 to 7, as detected by high-resolution radiosonde measurements at 12:00 UTC during the period of 2018–2019: **(a)** annual, **(b)** March–April–May (MAM), **(c)** June–July–August (JJA), **(d)** September–October–November (SON), and **(e)** December–January–February (DJF). Also marked is the probability for the specified cloud type at the top of each bar.

nomenon can be explained by the combined effects of low temperature and upward-motion conditions in winter, which promote the condensation or collision–coalescence of water vapor to form cloud droplets at relatively low altitudes during the ascending motion, resulting in low cloud bases (Dong et al., 2005; Chi et al., 2022). This results in the occurrence of CBH generally peaking in boreal summer (JJA) and boreal spring (MAM) and reaching its lowest value in boreal winter (DJF) and boreal autumn (SON), which is in good agreement with previous studies (e.g., Dong et al., 2005; Xi et al., 2010; Zhang et al., 2019).

Different from CBH, the occurrence frequencies of CTH exhibit a bimodal distribution, with a lower peak between 0.5 and 3.0 km and an upper peak between 6 and 12 km (Fig. 8b and e), which agrees with previous studies based on ground-based lidar and radar measurements (Comstock and Jakob, 2004). The occurrence frequency of CTH reaches a maximum at around 11 km, which is slightly lower than the corresponding global-annual-mean tropopause height (almost 12 km), and then it decreases rapidly with altitude. Above 9 km, the maximum occurrence frequency of CTH occurs in boreal summer (JJA), which is due to the deeper troposphere and the higher frequency of deep convective clouds in summer (Johnson et al., 1999; Zhang et al., 2019). This result is consistent with that reported by Zhang et al. (2019), which demonstrated that CTH peaked around in summer. Below 3 km, the occurrence frequency of CTH is the highest in boreal winter (DJF). The occurrence frequencies of CTH tend to increase with altitude between 3 and 9 km, irrespective of season.

As for CTH, the vertical distribution of cloud occurrence frequency is distinctly bimodal but in different ranges of altitude, namely, a lower peak between 0.5 and 3 km and a higher peak between 6 and 10 km (Fig. 8c and f). These findings are in line with previous studies (e.g., Mace and Benson, 2008; Zhang et al. 2014), which reported that the vertical profile of cloud occurrence peaked both in the boundary layer and upper troposphere by analyzing cloud retrievals from radiosondes, models, and satellites at both regional and global scale. Above 6 km, more clouds occur in boreal summer (JJA) than in other seasons, while below 3 km, there are more clouds in boreal winter (DJF).

To further study the characteristics of CVS over different regions of the world, the vertical distributions of the occurrence frequencies of CBH, CTH, and cloud over six regions of interest (ROIs; Fig. 1) at 12:00 UTC are shown in Figs. 9, 10, and 11. The regional-annual-mean PBLH and tropopause height as functions of longitude and latitude are also shown. Similar to the results of global-mean CBHs (Fig. 8a and d), the maximum occurrence frequencies of regional-mean CBHs are also within the regional-mean PBLH (Fig. 9a, b, c, g, h, and i). The occurrence frequencies of CBHs are nearly zero above the tropopause. The conditions that cloud bases above the tropopause are often in result from the overshooting tops from strong convective storms, such as deeply penetrating cumulonimbus and thunderstorms (Rosenfeld et al., 2007; Homeyer and Kumjian, 2015; Liu et al., 2021). Due to strong upward motion contained in the strong convective storms, the overshooting tops can reach as high as 19–20 km (Hassim et al., 2014). The frequency of cloud bases between
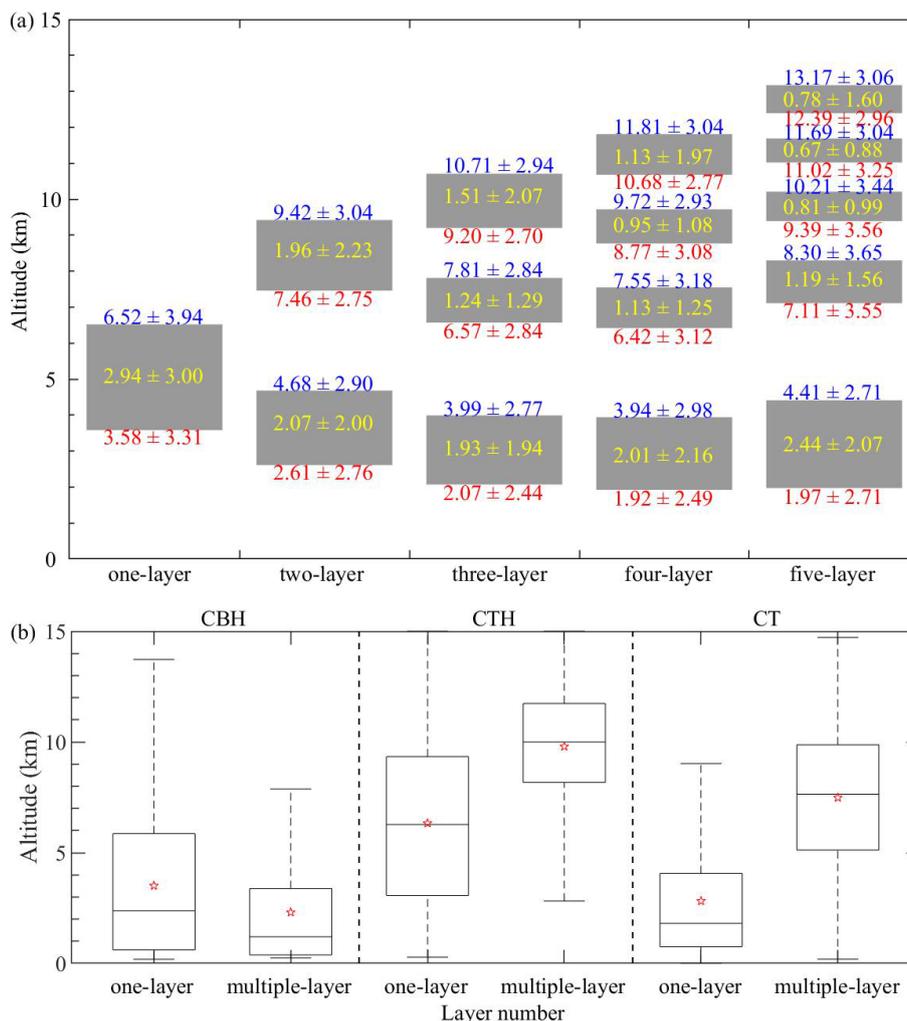
Figure 7. Near-global annual-mean **(a)** vertical locations of one-, two-, three-, four-, and five-layer clouds and **(b)** box plot of CVS (CBH, CTH, and CT) for one- and multi-layer clouds at 12:00 UTC during the period of 2018–2019. The mean ± 1 standard deviation values of CBH, CTH, and total CT for each cloud type are also marked in **(a)**.

1 and 3 km in East Asia is roughly larger than that over North America and Europe, which is consistent with previous studies (e.g., Zhang et al., 2013; Zhou et al., 2021; Sharma et al., 2022). The possible reason is that the air pollution issue in China is more severe, and the higher aerosol loading can change the macro- and microphysical properties of clouds and may invigorate convective clouds at high altitudes at the expense of low-level clouds (Wall et al., 2014; Guo et al., 2018; Liu et al., 2020). The variation pattern of CBH frequency with altitude in the Southern Hemisphere (SH) is similar to that in NH, but its fluctuation is roughly greater due to fewer stations available there. A close inspection of the horizontal distribution of CBHs shows that there is a pattern consisting of high values in the west and low values in the east in North America and a pattern of higher values in the north and lower in the south in China (Fig. 9e), which correspond to arid (high CBHs) and humid (low CBHs) cli-

mates there. Most (67 %) annual-mean CBHs range from 2 to 4 km with an average of 3.07 ± 1.06 km (Fig. 9d, e, and f).

The characteristics of CTHs over the six ROIs at 12:00 UTC are shown in Fig. 10. Similar to the global-mean CTHs, the regional-mean occurrence frequencies of CTHs above tropopause also decrease rapidly with altitude. As expected, most cloud tops are within the tropopause height in East Asia and North America. However, this predominance is not obvious in Europe and Antarctica, where the tropopause is lower since the climates are humid. In East Asia, the CTH frequency is generally highest in boreal summer (JJA) above 6 km since there is more frequent deep convective cloud during the summer monsoon (Wang et al., 2000), while it is highest in boreal winter (DJF) below 6 km as little solar radiation reaches the surface in winter, meaning that the cloud development is weak, and thus the CTH is relatively low. This result is in agreement with previous cloud radar ob-
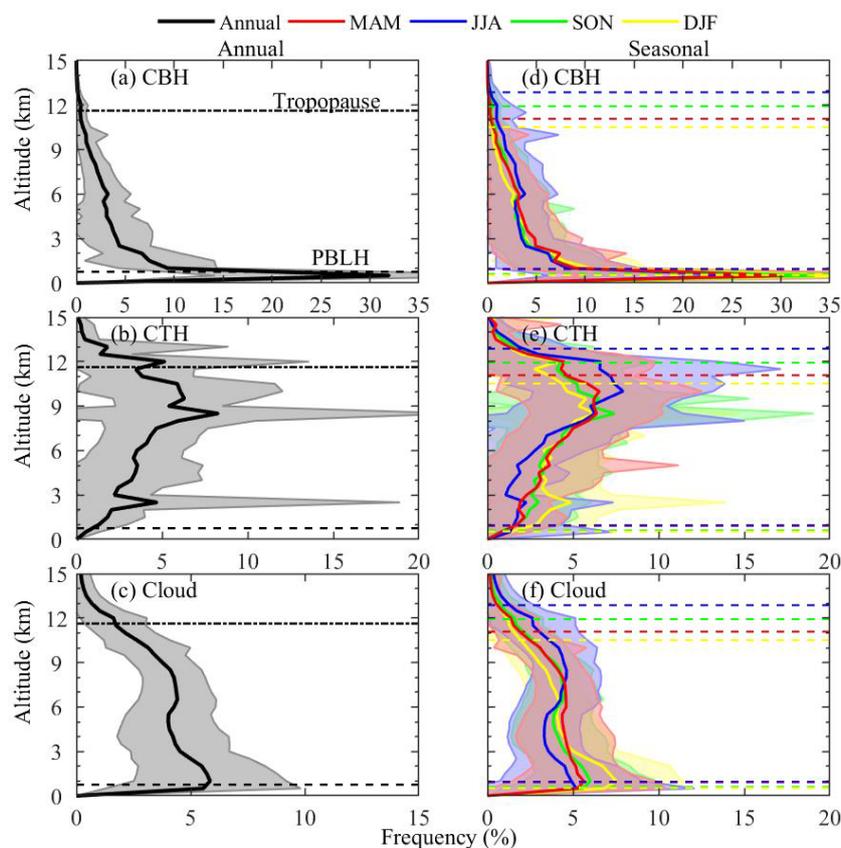
Figure 8. Near-global-mean vertical distributions of **(a, b, c)** annual and **(d, e, f)** seasonal occurrence frequencies of CBHs, CTHs, and clouds as detected by radiosonde data at 12:00 UTC during the period of 2018–2019, respectively. The annual, MAM, JJA, SON, and DJF periods are marked in black, red, blue, green, and yellow, respectively. Samples are vertically divided with a resolution of 500 m. The percentage for a given altitude is defined as the ratio of cloudy samples on that altitude to all cloudy samples. The solid lines are the mean values, and shadows are the 1 standard deviation at annual or a given season. The planetary boundary layer height (PBLH) is determined with the method proposed by Vogelezang and Holtslag (1996), marked by a dashed–dotted line, and the tropopause is defined with the method from WMO (1957), marked by a dashed line. The determination of PBLH and tropopause are detailed in the Supplement.

servations (Zhang et al., 2019). Relatively large CTHs occur in the southern United States and southeast China, which are affected by monsoons, resulting in more deep convective clouds (Fig. 10e). Note the mean CTHs in the tropical western Pacific are significantly larger than other regions, reaching up to 12 km. At this region, the occurrence frequency of subvisible cirrus is highest (data not shown). This can be explained by deep convection mostly occurring in tropical areas, favoring the formation of subvisible cirrus (Krämer et al., 2009; Froyd et al., 2010). These results are consistent with previous studies based on satellite observations (Martins et al., 2011; Schoeberl et al., 2022). Most (85 %) annual-mean CTHs vary from 7 to 12 km, with an average of 8.44 ± 1.52 km (Fig. 10d, e, and f).

The annual and seasonal mean occurrence frequencies of clouds at different regions are shown in Fig. 11. A bimodal distribution of the occurrence frequencies of clouds with altitude appears in North America and Europe, peaking at the top of the boundary layer (~ 1 km) and the tropopause (10–

11 km), while there is a unimodal distribution in East Asia, peaking at about 3 km; namely fewer clouds occur in the boundary layer compared to the result of global mean. This is attributed to more serious air pollution issues in East Asia compared to North America and Europe, resulting in higher occurrence frequencies of convective clouds at high altitudes (Liu et al., 2020; Sharma et al., 2022). This result is consistent with Xu et al. (2021a). Above 6 km in East Asia (~ 9 km at North America; ~ 10 km at Europe), the cloud occurrence frequency in JJA is higher than that in other seasons because of the deeper troposphere and the more frequent occurrence of convective storms in summer (Xi et al., 2010). Below 3 km in East Asia (~ 1 km in North America and Europe), the frequency of cloud occurrence in DJF is the highest, since stratus clouds usually occur in winter (Dong et al., 2005). In Antarctica, the peak of cloud occurs at low altitude (~ 1 km; a little bit higher than the PBLH ~ 0.70 km) due to the cold climate there. Contrary to CBHs, the annual-mean CTs have a pattern consisting of lower values in the west and higher
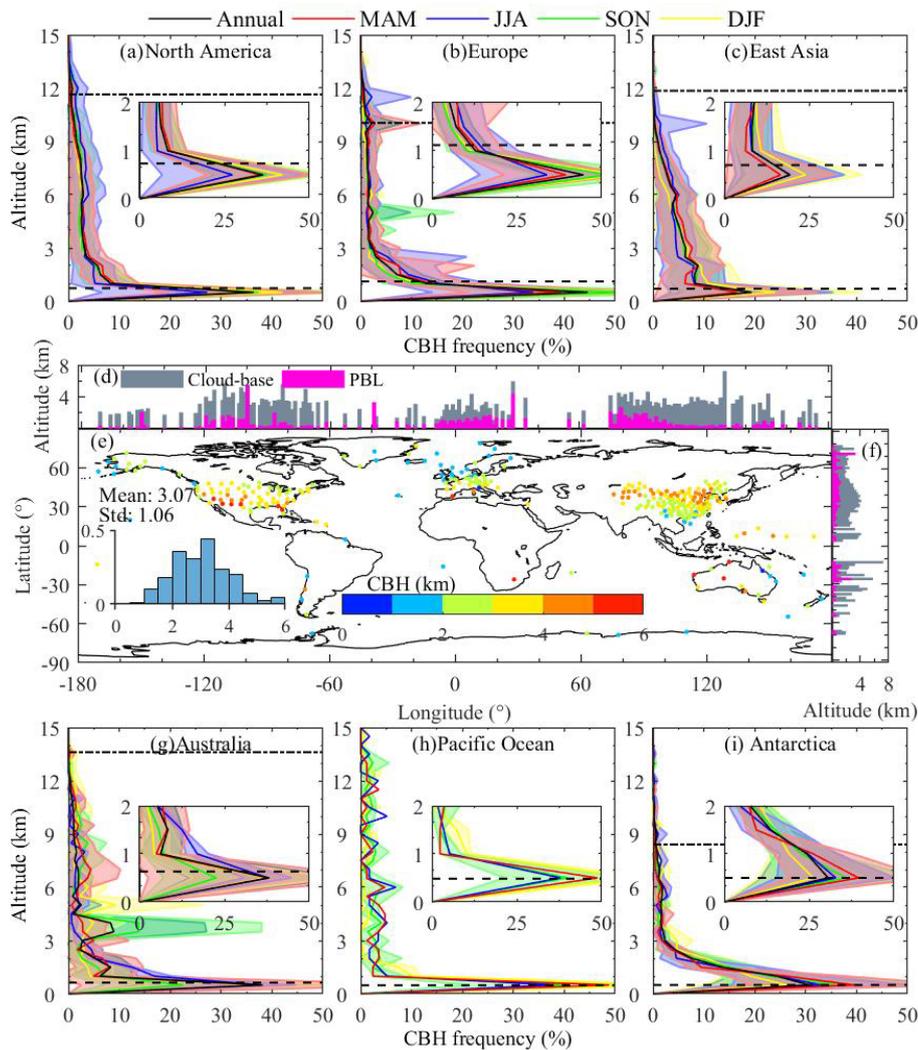
Figure 9. Regional-mean vertical distributions of the occurrence frequencies of CBHs at 12:00 UTC during the period of 2018–2019. The altitude-resolved annual and seasonal averaged occurrence frequencies of CBHs are displayed in **(a, b, c, g, h, i)** over six regions of interest, including North America, Europe, East Asia, Australia, the Pacific Ocean, and Antarctica. Also shown are the near-global geographic distribution of the annual-mean CBH **(e)**, with the histogram of the probability distribution for CBH in the inset and the corresponding meridional **(d)** and zonal **(f)** means overlaid with the mean PBLH.

values in the east in North America and a pattern with lower values in the northwest and higher values in the southeast in East Asia. Relatively large CTs exist in Europe since there is sufficient water vapor for cloud development under the oceanic climate. The CTs in the 20–30° zone are relatively smaller (Fig. 11f) because they coincide with the mean subsidence zone of the Hadley circulation (Poore et al., 1995). Most (52 %) annual-mean CTs vary from 4 to 6 km, with an average of 5.37 ± 1.58 km (Fig. 11d, e, and f).

The corresponding near-global and regional mean vertical distributions of occurrence frequencies of CVS at 00:00 UTC on annual and seasonal timescales (Figs. S4, 5, 6, 7, and 8) are similar to those at 12:00 UTC.

3.4 Near-global horizontal distribution of cloud

Figure 12 presents the horizontal distribution of the annual-mean occurrence frequencies for different layer clouds. Generally, more clouds occur in humid climate regions (e.g., eastern United States, southern China, and western Europe) (Fig. 12a). This is due to sufficient water vapor supply from the surface and also due to clouds being able to be generated if aerodynamic and thermodynamic conditions required for cloud decoupling are met. Similarly, the wetter the climate, the higher the occurrence frequencies of clouds for three-, four-, and five-layer clouds in cloudy skies (Fig. 12d, e, and f). Conversely, more one-layer clouds in cloudy skies occur in regions with a relatively arid climate compared to the humid climate regions (Fig. 12b). Reddy et al. (2018) re-
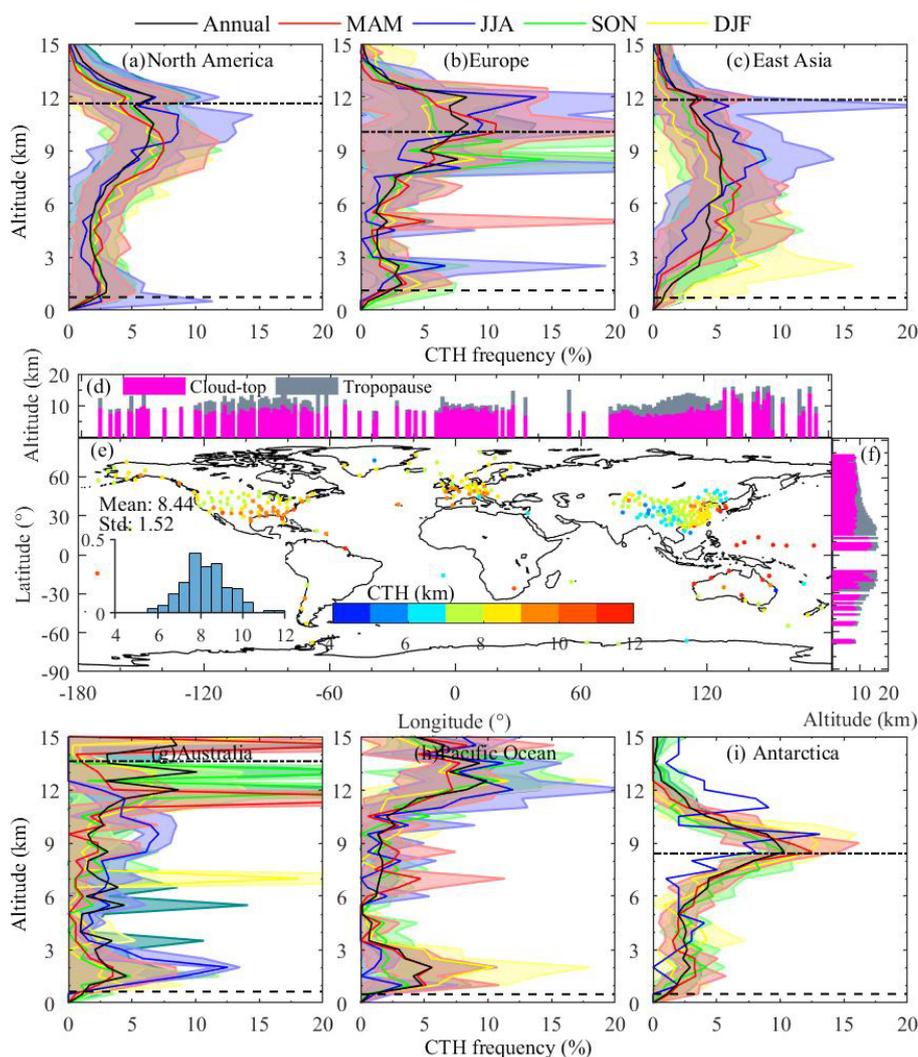
Figure 10. Similar to Fig. 9 but for the occurrence frequencies of CTHs at 12:00 UTC during the period of 2018–2019.

ported that the occurrence of multi-layer clouds was more significant under moist atmospheric conditions, while more one-layer clouds occurred under dry atmospheric conditions. As the transition between one- and multi-layer clouds, the spatial feature of two-layer clouds (Fig. 12c) is not apparent compared to other cloudy conditions. Spatially, more one-layer clouds occur over Asia than in North America (Fig. 12b), while there are roughly larger cloud frequencies for multi-layer clouds over North America (Fig. 12c, d, and f). These results are consistent with Wang et al. (2000), which demonstrated that the frequency of multi-layer clouds was higher in North America than in Asia. Few studies provided the global spatial distribution of the occurrence frequencies of clouds with various number of layers (from one- to five-layer) by radiosonde measurements as shown in Fig. 12.

Figure 13 shows the horizontal distributions of the near-global CBH, CTH, and CT at 12:00 UTC. In terms of seasonality, the CBHs in boreal winter (DJF) vary lit-

tle with space compared to other seasons. The magnitudes of CBH follow the order of boreal summer (JJA: 3.74 ± 1.56 km) > autumn (SON: 3.08 ± 1.22 km) $\approx$ spring (MAM: 3.05 ± 1.11 km) > winter (DJF: 2.55 ± 1.02 km) (Fig. 13a, b, c, and d). This result is consistent with previous satellite observations that the CBHs reached their maximum in summer and minimum in winter (Chi et al., 2022). This could be explained by the fact that more solar radiation energy is available for cloud development in summer (Zhang et al., 2018). In East Asia, the CBHs exhibit a pattern with high values in the northwest and low values in the southeast; namely, high clouds (as high as 4.0 km) tend to occur in northwest China, while low clouds (less than 2.0 km) tend to occur in southeast China and the northern part of the South China Sea (Fig. 13a, b, c, and d). This phenomenon further illustrates that a humid (arid) climate tends to generate low (high) clouds. The reason may be that the higher dewpoint in humid climate regions always causes
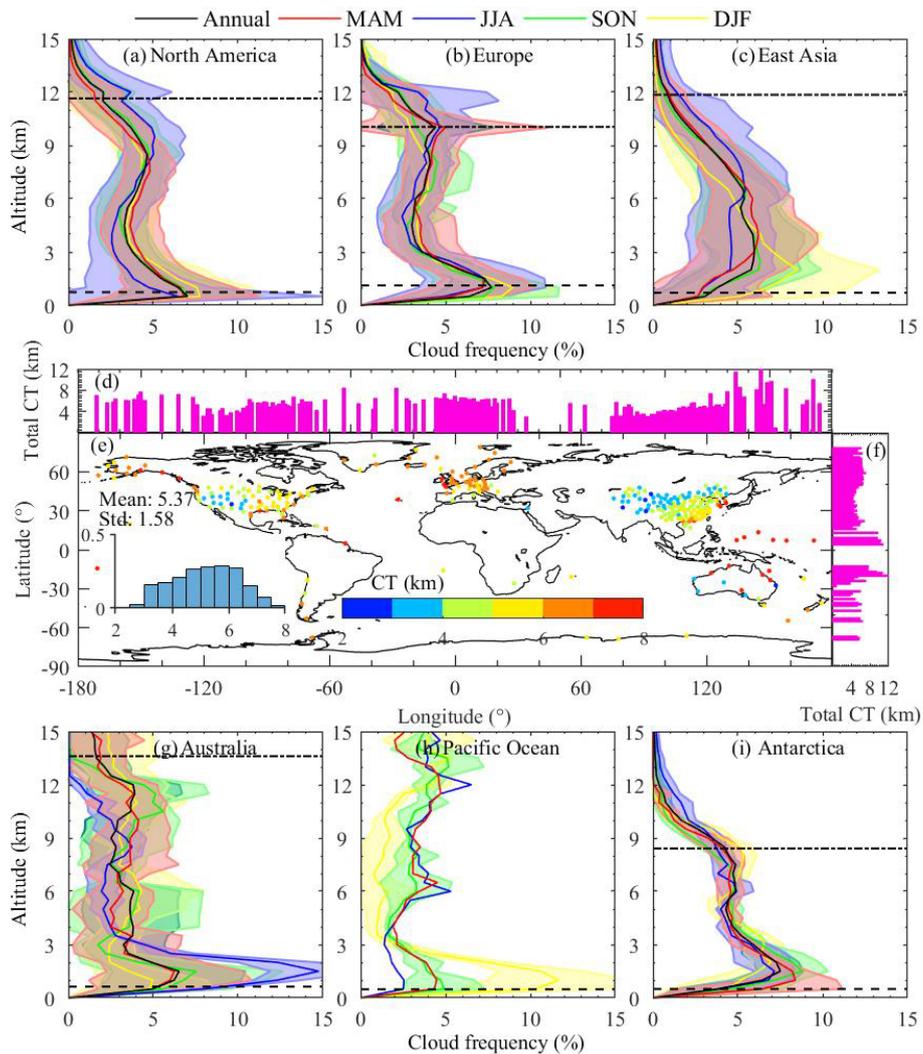
Figure 11. Similar to Fig. 9 but for the occurrence frequencies of clouds at 12:00 UTC during the period of 2018–2019.

a lower LCL, resulting in lower cloud bases (Zhang et al., 2018). Similarly, in North America, the CBHs are lower in the east and higher in the west, which is consistent with the results of An et al. (2017) based on the information from the Automated Surface Observing System Observation for a 5-year period (2008–2012). This can be explained by the fact that the western United States is often dry near the surface, and thus PBLHs tend to be much deeper, resulting in higher CBHs compared to eastern USA.

For CTH, its relative magnitudes have the same seasonality as those for CBH; namely, a higher CBH occurs in boreal summer (JJA: 9.24 ± 1.67 km), and a relatively lower value occurs in boreal winter (DJF: 7.63 ± 2.05 km) (Fig. 13e, f, g, and h). This is because more deep convective clouds occur in summer as opposed to other reasons (Johnson et al., 1999; Zhang et al., 2019). During boreal summer (JJA), the spatial distribution of CTHs exhibits an obvious pattern with high values in the southeast and low values in the northwest

in China and a pattern with high values in the east and low values in the west in the contiguous United States. The phenomenon of the pattern consisting of high values in the southeast and low values in the northwest in China is highly related to the East Asia summer monsoon, which causes strong atmospheric convection in southeastern China and makes the convective instability layer much thicker. This allows the water vapor to be transported to a higher altitude and favors the production of deep convective clouds (Sun et al., 2019; Chi et al., 2022). The pattern of high CTH values in the east and low CTH values in the west in the contiguous United States is attributed to the humid (arid) climate in the east (west) of the United States.

The CT values (Fig. 13i, j, k, and l) undergo almost the same seasonality with the CBHs and CTHs, with the order of JJA (5.50 ± 1.89 km) > SON (5.23 ± 1.58 km) $\approx$ MAM (5.20 ± 1.59 km) > DJF (5.08 ± 1.96 km). The spatial pattern of CT is similar to that of CTH, with larger CT in the humid
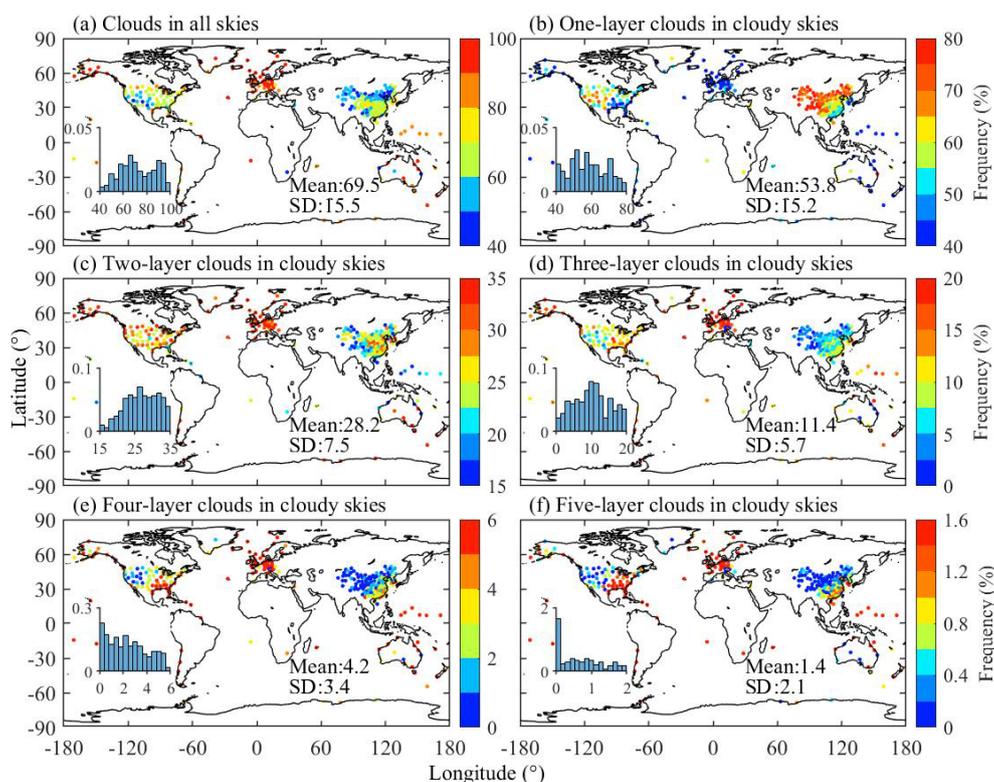
Figure 12. The geographic distributions of the occurrence frequencies of **(a)** clouds in all skies and **(b, c, d, e, f)** one-, two-, three, four-, and five-layer clouds in cloudy skies at 12:00 UTC during the period of 2018–2019. It should be noted that the range of the color bar differs a lot in order to improve the visual interpretation. Also shown are the histograms of probability distributions for the cloud occurrence frequencies in each panel.

climate regions and smaller CT in the arid climate regions. The reason is that higher RH not only contributes to a lower cloud base but also helps an air parcel to reach higher levels and thus leads to larger cloud thickness (Zhang and Klein, 2013). Interestingly, the CTs in Europe are relatively large compared to those in China and the United States. As mentioned before, this is partly explained by oceanic climates dominating in Europe, where more water vapor supply is available for cloud development.

Overall, the spatial distributions of CVS characteristics in different seasons are largely affected by the climates. The arid (humid) climates favor larger (smaller) CBH and smaller (larger) CTH and CT. The corresponding results of CVS at 00:00 UTC are roughly close to those at 12:00 UTC, as shown in Figs. S9 and 10.

3.5 Diurnal variation of cloud occurrence frequency at various heights

Since near-global radiosonde sites cover almost all time zones, the diurnal cycle of cloud vertical structures can be obtained by converting UTC to local solar time (LST). Based on the radiosonde-derived CVS, the diurnal variations of height-resolved occurrence frequencies of clouds in boreal summer

(JJA) and boreal winter (DJF) are presented in Fig. 14. The mean vertical profiles of the occurrence frequency of liquid, ice, and mixed clouds at both 00:00 and 12:00 UTC are also shown for the corresponding season. Ice clouds are identified when T is below $-20\,°C$, liquid clouds are detected with T above $0\,°C$, and mixed clouds correspond to T between -20 and $0\,°C$, as described in Sect. 2.2.1.

In boreal summer, the maximum occurrence frequencies of clouds mainly appear at altitudes of 0.5–3 km, and the second peak extends upward to be 6–10 km (Fig. 14b). The lower peak of the cloud occurrence frequency (0.5–3 km) roughly corresponds to the peak of the liquid cloud occurrence frequency (0.5–3 km), while the upper peak of the cloud occurrence frequency (6–12 km) roughly corresponds to the combined peak of the ice (8–12 km) and mixed-cloud occurrence frequencies (6–8 km), as shown in Figs. 14b and c and 8c and f. Note that a vertical distribution of liquid and ice cloud occurrence frequencies is expected, since T tends to decrease as altitude increases, and, thus, ice clouds tend to be generated at higher altitude compared to liquid clouds. Previous studies also reported that ice clouds were located higher than liquid clouds based on satellite data (Chang and Li, 2005). In particular, in the tropical and midlatitudes, subvisible cirrus clouds can reach to the upper tropopause (Gierens
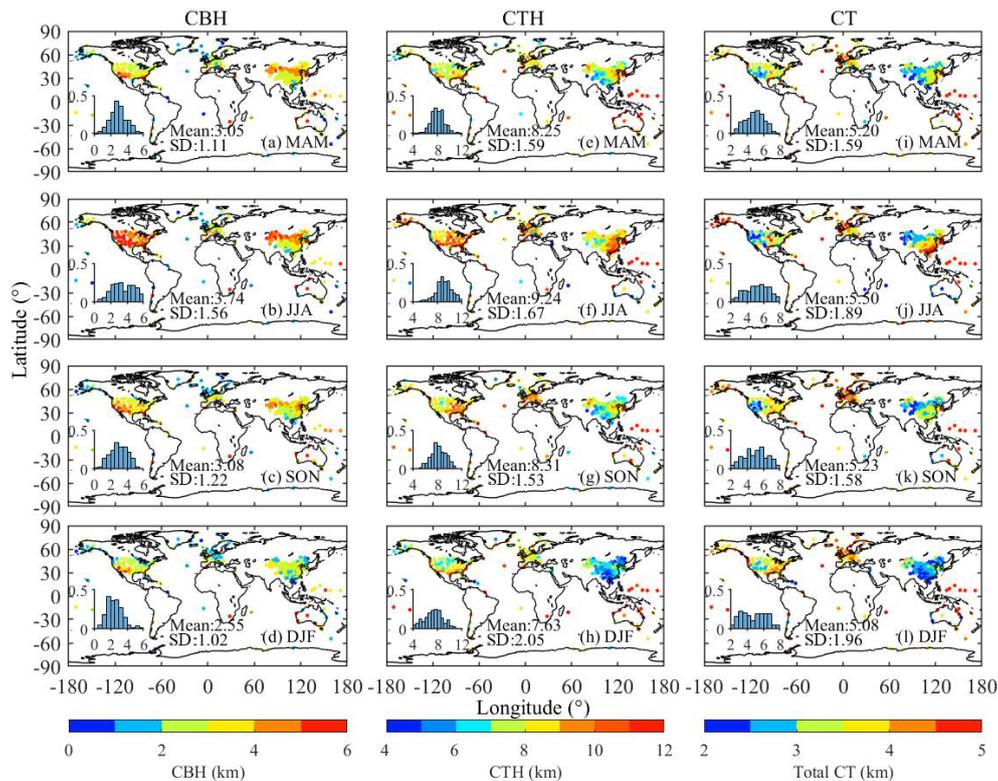
Figure 13. The geographic distributions of the seasonal mean CBH **(a, b, c, d)**, CTH **(e, f, g, h)**, and CT **(i, j, k, l)** at 12:00 UTC during the period of 2018–2019. Also shown are the histograms of probability distributions for the CVS in each panel.

and Spichtinger, 2000; Immler et al., 2008). Subvisible cirrus generally occurs in the ice-supersaturated regions and can form in situ or as a consequence of deep convection (Krämer et al., 2009; Froyd et al., 2010). The clouds in the lower atmosphere tend to appear as the sun rises and increases from morning to early afternoon (15:00 LST) within 3 km altitude. The reason is that, during daytime solar radiation heats the surface and drives turbulence and convection in the boundary layer, which largely affects the boundary layer clouds (Noel et al., 2018). In the late afternoon (16:00–18:00 LST), clouds tend to form most frequently at relatively high altitudes (6–12 km), which is consistent with Chen et al. (2018). The reason may be that after solar radiation reaches a peak, the sun heats less, and the cloud top begins to cool, which increases the atmospheric instability and fuels the development of one-layer cloud and the uppermost layer of cloud (Zhang et al., 2010). These findings are consistent with those reported by Chang and Li (2005), who analyzed satellite cloud retrievals on a global scale. After 18:00 LST, clouds tend to occur below 3 km again.

For boreal winter, clouds mainly occur with maximum frequencies at altitudes of 0.5–3 km, which roughly corresponds to the combined peak of the liquid (0.5–3 km) and mixed-cloud occurrence frequencies (0.5–6 km), as shown in Figs. 14e and f and 8c and f. Note that there is a relatively large occurrence frequency of clouds during 06:00–

08:00 LST, which is consistent with Betts and Tawfik (2016), who demonstrated that clouds had a near-sunrise peak in the cold season. The reason may be that the air temperatures are lowest around sunrise for a stable boundary layer, which is beneficial for water vapor to accumulate and form cloud (e.g., Dai, 2001; Eastman and Warren, 2014; Gao et al., 2019; An et al., 2017, 2020).

In boreal spring and autumn, the characteristics of the diurnal variations of cloud occurrence frequencies fall between those in boreal summer and winter. The diurnal variation of height-resolved occurrence frequencies of clouds provided by this study can be a reference for satellite-retrieved CVS products, even though the sampling at each hour is not even (Fig. 14a and d).

3.6　Association of CBH with meteorological variables and moisture

We further investigate the potential key factors linked to CBH, since CBH is one of the most important factors affecting CRE in numerical weather forecasts and regional climate models (Kato et al., 2011; Viúdez-Mora et al., 2015; Prein et al., 2015). Previous studies suggested that CBH is affected by thermodynamic conditions (e.g., surface T, RH, and PS) and large-scale dynamic processes (wind speed) in the near-surface layer and moisture conditions (Mauger and
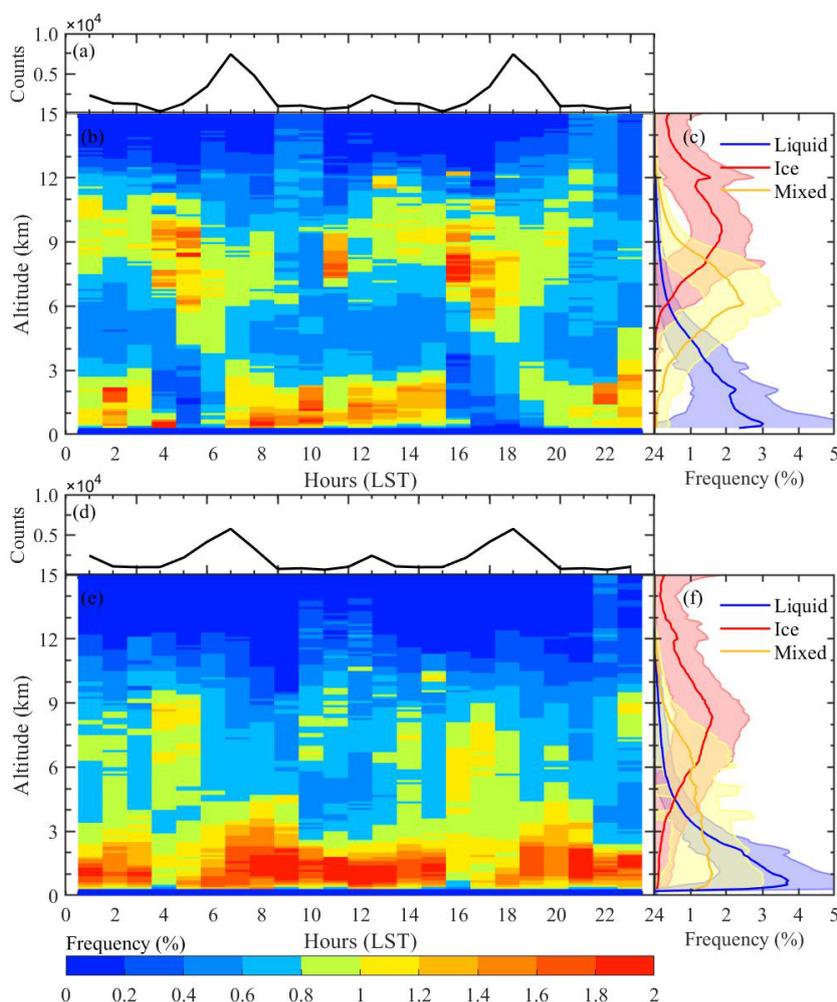
Figure 14. Diurnal variations of all clouds and altitude-resolved clouds as detected by all radiosondes at 00:00 and 12:00 UTC in boreal summer (JJA; **a, b**) and boreal winter (DJF; d and e) during the period of 2018–2019. Also shown are the vertical probability distributions of liquid (in blue), ice (in red), and mixed liquid–ice (in yellow) clouds in boreal summer and boreal winter **(c, f)**.

Norris, 2010; Gbobaniyi et al., 2011). In this study, we investigate the relationship of CBH with meteorological variables ($T_{2\,m}$, PS, $RH_{2\,m}$, and $WS_{10\,m} = \sqrt{u^2 + v^2}$, where WS is wind speed) and moisture (θ and MFD).

The spatial distributions of the correlation relationships between CBH and meteorological variables are displayed in Fig. 15. Each point is the R value of a given CBH and meteorological variable at 12:00 UTC over 2018–2019. Also given are the mean value and 1 standard deviation of the R values on a global scale, which is obtained by averaging the absolute R value of each station. Generally, the magnitudes of the global-mean absolute R values follow the order of R (CBH & $RH_{2\,m}$) = 0.29 ± 0.17 > R (CBH & $T_{2\,m}$) = 0.22 ± 0.16 > R (CBH & PS) = 0.17 ± 0.14 > R (CBH & $WS_{10\,m}$) = 0.15 ± 0.13. Since the CBH is detected using the profiles of T and RH, it is reasonable to expect that the correlation between CBH and $T_{2\,m}$ and $RH_{2\,m}$ is relatively high. Our result is consistent with Gbobaniyi et al. (2011),

who demonstrated that surface temperature and specific humidity were strongly coupled with CBH. Interestingly, the CBHs are negatively related with $RH_{2\,m}$, while they are positively related with $T_{2\,m}$, which further convinces us that humid and cold climates tend to generate low clouds. The physical explanation could be that, compared to dry air, humid air tends to reach condensation at relatively low altitude; thus the corresponding CBH is low. Note that the correlation between $T_{2\,m}$ ($RH_{2\,m}$) and CBH tends to be larger in northern China compared to the other regions of China. This is attributed to the combined effects of the larger $T_{2\,m}$ and smaller $RH_{2\,m}$, resulting in larger CBH (as shown in Fig. 13a, b, c, and d). Compared with $T_{2\,m}$ and $RH_{2\,m}$, the correlation between CBH and PS and $WS_{10\,m}$ is relatively weaker (most of absolute $R < 0.3$). Note that the correlation of CBH and $WS_{10\,m}$ is negative in southeastern China but positive in northwestern China. The reason may be that the climate of southeastern China is mainly affected by monsoon, and the large WS

brings more humid air, causing lower cloud bases, while the air is relatively dry in the northwestern China, a region that is largely affected by the high pressure from Siberia, and a large WS brings more dry air, corresponding to higher cloud bases.

Figure 16 shows the spatial distributions of the correlation relationships between CBH and soil moisture (θ, Fig. 16a) and MFD (Fig. 16b). Obviously, most CBHs are negatively correlated to θ, with mean absolute R (CBH & θ) $= 0.22 \pm 0.15$. This suggests that large soil moisture corresponds to low CBH, since more surface-available energy is partitioning to the latent heat flux with high soil moisture, causing a reduced boundary layer height. Thus, clouds are generated with low bases (Betts, 2004; Cook et al., 2006; Huang and Margulis, 2013). The correlation of MFD with CBH is relatively weak, with most R values ranging from -0.1 to 0.1 (Fig. 16b). This is not surprising since CBH is not significantly affected by the transportation of water vapor. Overall, the correlation between CBH and $RH_{2\,m}$ is the strongest, followed by $T_{2\,m}$, θ, PS, and $WS_{10\,m}$, and the correlation with MFD is the weakest.

To further obtain a quantitative understanding of the effects of meteorological variables and moisture on CBH, the 2D joint distribution of CBH is presented in Fig. 17. At given $T_{2\,m}$, larger $RH_{2\,m}$ corresponds to lower CBH, while at given $RH_{2\,m}$, larger $T_{2\,m}$ tends to result in higher CBH (Fig. 17a). Besides, the combined effect of $T_{2\,m}$ and $RH_{2\,m}$ on the variation of CBH shows that larger $T_{2\,m}$ and smaller $RH_{2\,m}$ result in higher CBH. The same as Fig. 16, the CBH varies slightly as MFD changes, indicating that MFD exerts little impact on CBH. Different with MFD, larger θ is attributed to lower CBH when $\theta > 0.2\,m^3\,m^{-3}$. However, CBH is not sensitive to low θ. The relationship of CBH with meteorological variables and soil moisture at 00:00 UTC (Figs. S11, 12, and 13) is similar to that at 12:00 UTC.

4   Summary and conclusions

Based on high-vertical-resolution radiosonde observations from 374 near-global radiosonde stations, 2 years' worth (2018–2019) of near-global, high-quality CVS has been determined. A novel retrieval method is developed which combines the vertical gradients of T and RH and the altitude-resolved thresholds of RH. The accuracy of radiosonde-derived CVS is assessed by comparison with MMCR measurements at Beijing site during the year of 2019. The good agreement in CBHs ($R = 0.91$) and CTHs ($R = 0.81$) confirms that this retrieval method performs reasonably well. On a global scale, the CBHs from ERA5 tend to be lower than those from radiosondes, with R values of 0.24 and 0.49 at 00:00 and 12:00 UTC, respectively. The characteristics of near-global CVS are summarized in the following.

The near-global annual-mean occurrence frequency of all clouds is 65.3 % (69.5 %) at 00:00 (12:00) UTC, which is close to the result from multiple satellite observations (68.0 % ± 3.0 %). Over cloudy skies, the cloud frequency decreases as the number of cloud layers increases. The one-layer clouds are predominant, accounting for 55.4 % (53.8 %) of all cloud configurations. Among the detected multi-layer clouds, 62.2 % (61.1 %) are two-layer clouds at 00:00 (12:00) UTC. More clouds occur in boreal winter (DJF) and spring (MAM) than in summer (JJA) and autumn (SON).

The CBH and CT of each cloud layer (CTH) tend to decrease (increase) as the number of cloud layers increases. For one-layer clouds, they are roughly located at altitudes that fall somewhere among the altitudes of the multi-layer cloud configurations, and their thicknesses are greater than those of any layer of multi-layer clouds. For multi-layer clouds, the lowermost cloud layer almost occurs below 3 km with small variation, while the upper layer exhibits more significant variation. The maximum altitude difference between cloud layers is around 2.5 km, which exists between the first and second layer for the three- and multi-layer cloud configurations. For the upper layers, the altitude difference decreases to be about 1.0 km.

In most cases, CBHs are located within 1 km, with the highest frequency at 0.5 km, which is lower than the global-annual-mean PBLH (0.76 km). This result indicates that most of the time, cloud bases are in the atmospheric boundary layer. The vertical distributions of the CTH occurrence frequencies have two peaks with the upper peak at around 11 km, slightly lower than the global-annual-mean tropopause height (11.76 km). Similar to CTHs, the cloud occurrence frequencies also exhibit a bimodal distribution, with a lower peak being between 0.5 and 3 km and an upper peak being between 6 and 10 km, agreeing well with previous studies based on radiosondes, models, and satellites at both regional and global scale. Regionally, the occurrence frequencies of CBH in East Asia between 1 and 3 km are generally larger than those over North America and Europe, probably due to the severe air pollution issue in East Asia that invigorates convective clouds at high altitudes, which suppresses the occurrence of low-level clouds. The mean CTHs are highest in the tropical western Pacific, where subvisible cirrus mostly occurs.

As for the horizontal distribution of CVS, we find that there are more clouds in humid climate regions (e.g., eastern United States, southern China, and western Europe) since sufficient water vapor supply from the surface benefits the generation of clouds. More one-layer clouds occur in arid climate regions, while more clouds with more than two layers occur in humid climate regions. Compared to one-layer clouds and multi-layer clouds, there is no apparent spatial feature for two-layer clouds.

The global-mean CBH, CTH, and CT are 3.15 ± 1.15 (3.07 ± 1.06), 8.04 ± 1.60 (8.44 ± 1.52), and 4.89 ± 1.36 (5.37 ± 1.58) km at 00:00 (12:00) UTC, respectively. The CBH, CTH, and CT have almost the same seasonality, with
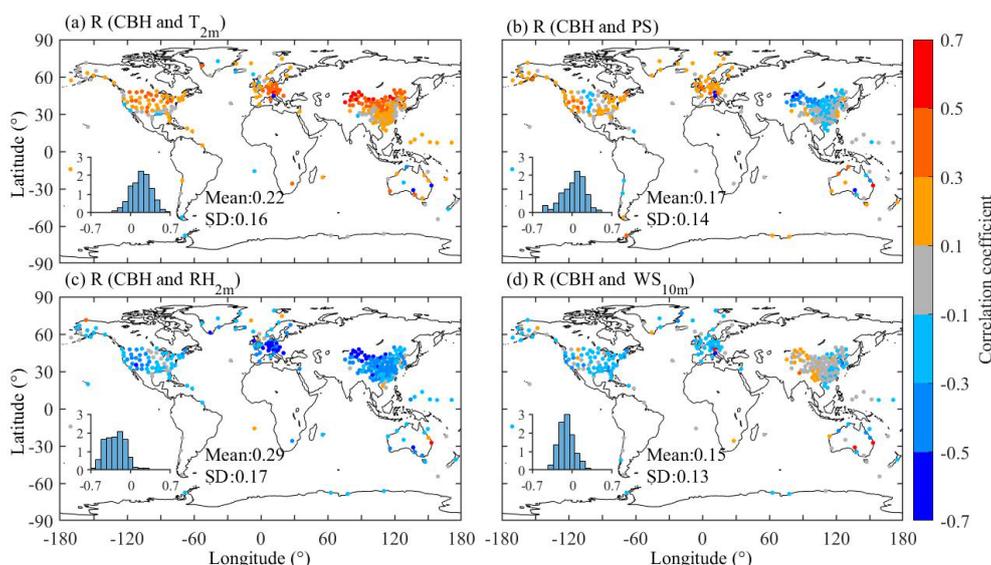
Figure 15. Geographic distributions of the correlation coefficients (R values) between radiosonde-derived CBH and surface meteorological variables: **(a)** 2 m air temperature ($T_{2\,m}$), **(b)** surface pressure (PS), **(c)** 2 m relatively humidity ($RH_{2\,m}$), and **(d)** 10 m wind speed ($WS_{10\,m}$) at 12:00 UTC during the period of 2018–2019. Also shown are the histograms of probability distributions for their corresponding R values in each panel.
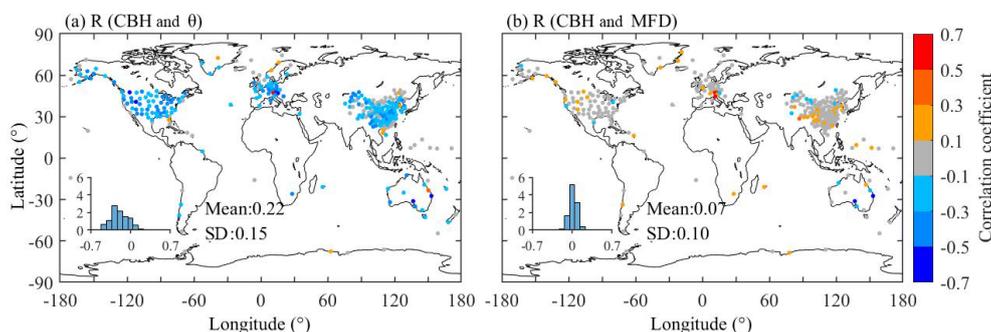
Figure 16. The same as Fig. 15 but for the correlations between CBH and **(a)** soil water content (θ) and **(b)** moist flux divergence (MFD) at 12:00 UTC during the period of 2018–2019.

magnitudes following the order of boreal summer > autumn ≈ spring > boreal winter. The spatial distributions of CVS are largely affected by the climate; namely, the arid (humid) climates correspond to larger (smaller) CBH and smaller (larger) CTH and CT.

In terms of the diurnal variation of cloud occurrence frequency, in boreal summer the maximum cloud occurrence frequencies mainly appear at altitudes of 0.5–3 km, corresponding to the peak of the occurrence frequencies of liquid clouds, and the second peak extends upwards to be 6–12 km, corresponding to the combined peak of the occurrence frequencies of ice and mixed clouds. During daytime, clouds are affected by solar radiation, tending to increase from morning to early afternoon (15:00 LST) within 3 km altitude, peak in the late afternoon (16:00–18:00 LST) at relatively high altitude (6–12 km), and then decrease after 18:00 LST. In boreal

winter, clouds are relatively low, with maximum frequencies appearing at altitudes of 0.5–3 km, corresponding to the combined peak of liquid- and mixed-cloud occurrence frequencies. And the clouds have a peak during the period 06:00–08:00 LST, associated with the lowest temperature around sunrise, which is beneficial for water vapor to accumulate and form clouds. The seasonal diurnal variations of cloud occurrence frequency are in accordance with those from satellite and ground measurements.

As for the correlation of CBH with meteorological variables and moisture, we find that the CBH is correlated with both the $RH_{2\,m}$ and $T_{2\,m}$, with global-mean absolute R values of 0.29 ± 0.17 and 0.22 ± 0.16, respectively. That is, larger air temperature and smaller humidity tend to result in larger CBH. Most CBH is negatively correlated to soil moisture, with a global-mean absolute R value of 0.22 ± 0.15, indi-
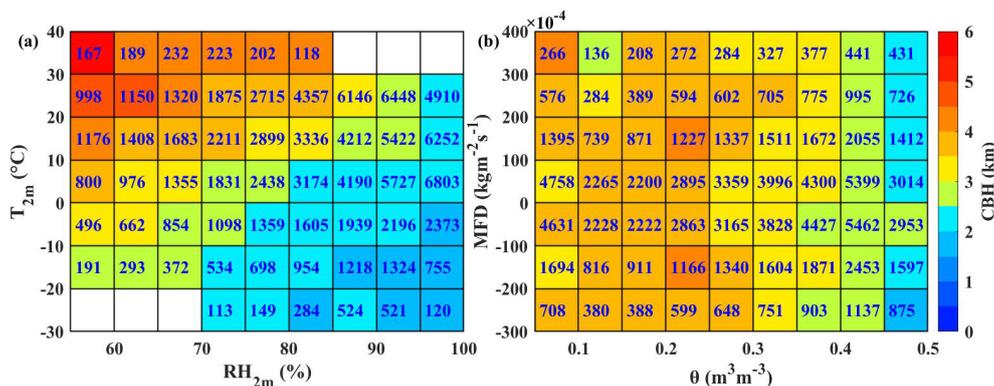
Figure 17. Joint dependences of CBH on **(a)** $T_{2\,m}$ and $RH_{2\,m}$ and **(b)** θ and MFD at 12:00 UTC during the period of 2018–2019. The number labeled in each cell represents its corresponding sample size.

cating that larger soil moisture corresponds to lower cloud bases. The relationship between CBH and moisture flux divergence is weak.

This study is the first attempt to characterize the near-global CVS from high-vertical-resolution radiosonde data. These results of CVS could be used to validate output from global climate models, as constraints for cloud formation would need to be done inside a parameterization. In addition, these results can also be readily used by the operational weather community given the widespread use of radiosondes in day-to-day forecasting operations. The formation mechanisms of cloud are complex, so studying features affecting the CVS appears to be a promising avenue for future work.

References

Ackerman, T. P., and Stokes, G. M.: The atmospheric radiation measurement program, Phys. Today., 56, 38–44, https://doi.org/10.1063/1.1554135, 2003.

An, N., Wang, K. C., Zhou, C. L., and Pinker, R. T.: Observed variability of cloud frequency and cloud-base height within 3600m above the surface over the contiguous United States, J. Climate, 30, 3725–3742, https://doi.org/10.1175/JCLI-D-16-0559.1, 2017.

An, N., Pinker, R. T., Wang, K. C., Rogers, E., and Zuo, Z. Y.: Evaluation of cloud base height in the North American Regional Reanalysis using ceilometer observations, Int. J. Climatol., 40, 3161–3178, https://doi.org/10.1002/joc.6389, 2020.

Austin, R. T., Heymsfield, A. J., and Stephens, G. L.: Retrieval of ice cloud microphysical parameters using the CloudSat millimeter-wave radar and temperature, J. Geophys. Res.-Atmos., 114, D00A23, https://doi.org/10.1029/2008JD010049, 2009.

Bartels, R., Beatty, J., and Barsky, B: An Introduction to Splines for use in Computer Graphics and Geometric Modeling, Morgan Kaufmann, Inc., San Francisco, California, ISBN 9781558604001, 1995

Bell, B., Hersbach, H., Simmons, A., Berrisford, P., Dahlgren, P., Horanyi, A., Munoz-Sabater, J., Nicolas, J., Radu, R., Schepers, D., Soci, C., Villaume, S., Bidlot, J. R., Haimberger, L., Woollen, J., Buontempo, C., and Thepaut, J. N.: The ERA5 global reanalysis: Preliminary extension to 1950, Q. J. Roy. Meteor. Soc., 147, 4186–4227, https://doi.org/10.1002/qj.4174, 2021.

Betts, A. K.: Understanding hydrometeorology using global models, B. Am. Meteorol. Soc., 85, 1673–1688, https://doi.org/10.1175/BAMS-85-11-1673, 2004.

Betts. A. K. and Tawfik, A. B.: Annual climatology of the diurnal cycle on the Canadian prairies, Font. Earth Sci., 4, 1, https://doi.org/10.3389/feart.2016.00001, 2016.

Bian, J. C., Chen, H. B., Vömel, H., Duan, Y. J., Xuan, Y. J., and Lü, D. R.: Intercomparison of humidity and temperature sensors: GTS1, Vaisala RS80, and CFH, Adv. Atmos. Sci., 28, 139–146, https://doi.org/10.1007/s00376-010-9170-8, 2011.

Cadeddu, M. P., Liljegren, J. C., and Turner, D. D.: The Atmospheric radiation measurement (ARM) program network of microwave radiometers: instrumentation, data, and retrievals, Atmos. Meas. Tech., 6, 2359–2372, https://doi.org/10.5194/amt-6-2359-2013, 2013.

Cady-Pereira, K. E., Shephard, M. W., Turner, D. D., Mlawer, E. J., Clough, S. A., and Wagner, T. J.: Improved daytime column-integrated precipitable water vapor from Vaisala radiosonde humidity sensors, J. Atmos. Ocean. Tech., 25, 873–883, https://doi.org/10.1175/2007JTECHA1027.1, 2008.

Cesana, G. and Chepfer, H.: How well do climate models simulate cloud vertical structure? A comparison between CALIPSO-GOCCP satellite observations and CMIP5 models, Geophys. Res. Lett., 39, L20803, https://doi.org/10.1029/2012GL053153, 2012.

Cesana, G. and Waliser, D. E.: Characterizing and understanding systematic biases in the vertical structure of clouds in CMIP5/CFMIP2 models, Geophys. Res. Lett., 43, 10538–10546, https://doi.org/10.1002/2016GL070515, 2016.

Chang, F. L. and Li, Z.: A near global climatology of single-layer and overlapped clouds and their optical properties retrieved from TERRA/MODIS data using a new algorithm, J. Climate, 18, 4752–4771, https://doi.org/10.1175/JCLI3553.1, 2005.

Chandra, A. S., Zhang, C. D., Klein, S. A., and Ma, H. Y.: Low-cloud characteristics over the tropical western Pacific from ARM observations and CAM5 simulations, J. Geophys. Res.-Atmos., 120, 8953–8970, https://doi.org/10.1002/2015JD023369, 2015.

Chen, C., Song, X. Q., Wang, Z. J., Wang, W. Y., Wang, X. F., Zhuang, Q. F., Liu, X. Y., Li, H., Ma, K., Li, X., Pan, X., Zhang, F., Xue, B., and Yu, Y.: Observations of atmospheric aerosol and cloud using a polarized Micropulse Lidar in Xi'an, China, Atmosphere, 12, 796, https://doi.org/10.3390/atmos12060796, 2021.

Chen, D. D., Guo, J. P., Wang, H. Q., Li, J., Min, M., Zhao, W. H., and Yao, D.: The cloud top distribution and diurnal variation of clouds over East Asia: Preliminary results from advanced Himawari imager, J. Geophys. Res.-Atmos., 123, 3724–3739, https://doi.org/10.1002/2017JD028044, 2018.

Chernykh, I. and Eskridge, R.: Determination of cloud amount and level from radiosonde soundings, J. Appl. Meteorol. Clim., 35, 1362–1369, https://doi.org/10.1175/1520-0450(1996)035<1362:DOCAAL>2.0.CO;2, 1996.

Chi, Y. L., Zhao, C. F., Yang, Y. K., Ma, S. S., and Yang, J.: Cloud macrophysical characteristics in China mainland and east coast from 2006 to 2017 using satellite active remote sensing observations, Int. J. Climatol., 42, 8984–9002, https://doi.org/10.1002/Joc.7790, 2022.

Clothiaux, E. E., Ackermann, T. P., Mace, G. C., Moran, K. P., Marchand, R. T., Miller, M. A., and Martner, B. E.: Objective determination of cloud heights and radar reflectivities using a combination of active remote sensors at the ARM CART sites, J. Appl. Meteorol., 39, 645–665, https://doi.org/10.1175/1520-0450(2000)039<0645:ODOCHA>2.0.CO;2, 2000.

Comstock, J. M. and Jakob, C.: Evaluation of tropical cirrus cloud properties derived from ECMWF model output and ground based measurements over Nauru Island, Geophys. Res. Lett., 31, L10106, https://doi.org/10.1029/2004GL019539, 2004.

Comstock, J. M., Protat, A., McFarlane, S. A., Delanoë, J., and Deng, M.: Assessment of uncertainty in cloud radiative effects and heating rates through retrieval algorithm differences: Analysis using 3 years of ARM data at Darwin, Australia, J. Geophys. Res.-Atmos., 118, 4549–4571, https://doi.org/10.1002/jgrd.50404, 2013.

Cook, B. I., Bonan, G. B., and Levis, S.: Soil moisture feedbacks to precipitation in southern Africa, J. Climate, 19, 4198–4206, https://doi.org/10.1175/JCLI3856.1, 2006.

Costa-Surós, M., Calbó, J., González, J. A., and Martin-Vide, J.: Behavior of cloud base height from ceilmeter measurements, Atmos. Res., 127, 64–76, https://doi.org/10.1016/j.atmosres.2013.02.005, 2013.

Costa-Surós, M., Calbó, J., González, J. A., and Long, C. N.: Comparing the cloud vertical structure derived from several methods based on radiosonde profiles and ground-based remote sensing measurements, Atmos. Meas. Tech., 7, 2757–2773, https://doi.org/10.5194/amt-7-2757-2014, 2014.

Crewell, S., Bloemink, H., Feijt, A., Garcia, S. G., Jolivet, D., Krasnov, O. A., van Lammeren, A., Lohnert, J., van Meijgaard, E.,

Meywerk, J., Quante, M., Pfeilsticker, K., Schmidt, S., Scholl, T., Simmer, C., Schroder, M., Trautmann, T., Venema, V., Wendisch, M., and Willen, U.: The BALTEX Bridge Campaign - An integrated approach for a better understanding of clouds, B. Am. Meteorol. Soc., 85, 1565–1584, https://doi.org/10.1175/BAMS-85-10-1565, 2004.

Dai, A.: Global precipitation and thunderstorm frequencies. Part II: Diurnal variations, J. Climate, 14, 1112–1128, https://doi.org/10.1175/1520-0442(2001)014<1112:GPATFP>2.0.CO;2, 2001.

Dong, X. P., Minnis, P., and Xi, B.: A climatology of midlatitude continental clouds from the ARM SGP central facility. Part I: low-level cloud macrophysical, microphysical, and radiative properties, J. Climate, 18, 1391–1410, https://doi.org/10.1175/JCLI3342.1, 2005.

Dong, X., Minnis, P., Xi, B., Sun-Mack, S., and Chen, Y.: Comparison of CERES-MODIS stratus cloud properties with ground-based measurements at the DOE ARM Southern Great Plains site, J. Geophys. Res.-Atmos., 113, D03204, https://doi.org/10.1029/2007JD008438, 2008.

DWD: Index of /climate_environment/CDC/observations_germany/ radiosondes/high_resolution/historical/, DWD [data set], https://opendata.dwd.de/climate_environment/CDC/ observations_germany/radiosondes/high_resolution/historical/, last access: 1 March 2022.

Dzambo, A. M. and Turner, D. D.: Characterizing relative humidity with respect to ice in midlatitude cirrus clouds as a function of atmospheric state, J. Geophys. Res.-Atmos., 121, 12253–12269, https://doi.org/10.1002/2015JD024643, 2016.

Eastman, R. and Warren, S. G.: Diurnal cycles of cumulus, cumulonimbus, stratus, stratocumulus, and fog from surface observations over land and ocean, J. Climate, 27, 2386–2404, https://doi.org/10.1175/JCLI-D-13-00352.1, 2014.

Froyd, K. D., Murphy, D. M., Lawson, P., Baumgardner, D., and Herman, R. L.: Aerosols that form subvisible cirrus at the tropical tropopause, Atmos. Chem. Phys., 10, 209–218, https://doi.org/10.5194/acp-10-209-2010, 2010.

Gao, C. C., Li, Y. Y., and Chen, H. W.: Diurnal variations of different cloud types and the relationship between the diurnal variations of clouds and precipitation in central and east China, Atmosphere, 10, 304, https://doi.org/10.3390/atmos10060304, 2019.

Gbobaniyi, E. O., Abiodun, B. J., Tadross, M. A., Hewitson, B. C., and Gutowski, W. J.: The coupling of cloud base height and surface fluxes: a transferability intercomparison, Theor. Appl. Climatol., 106, 189–210, https://doi.org/10.1007/s00704-011-0421-0, 2011.

George, G., Sarangi, C., Tripathi, S. N., Chakraborty, T., and Turner, A.: Vertical Structure and Radiative Forcing of Monsoon Clouds Over Kanpur During the 2016 INCOMPASS Field Campaign, J. Geophys. Res.-Atmos., 123, 2152–2174, https://doi.org/10.1002/2017JD027759, 2018.

Giangrande, S. E., Wang, D., Bartholomew, M. J., Jensen, M. P., Mechem, D. B., Hardin, J. C., and Wood, R.: Midlatitude oceanic cloud and precipitation properties as sampled by the ARM Eastern North Atlantic Observatory, J. Geophys. Res.-Atmos., 124, 4741–4760, https://doi.org/10.1029/2018JD029667, 2019.

Gierens, K. and Spichtinger, P.: On the size distribution of ice supersaturated regions in the upper troposphere and lowermost stratosphere, Ann. Geophys., 18, 499–504, https://doi.org/10.1007/s00585-000-0499-7, 2000.

Goff, J. A., and Gratch, S.: Low-pressure properties of water from −160 °F to 212 °F, Trans. Am. Soc. Heating Air-Cond., Eng., 52, 95–122, 1946

Gouveia, D. A., Barja, B., Barbosa, H. M. J., Seifert, P., Baars, H., Pauliquevis, T., and Artaxo, P.: Optical and geometrical properties of cirrus clouds in Amazonia derived from 1 year of ground-based lidar measurements, Atmos. Chem. Phys., 17, 3619–3636, https://doi.org/10.5194/acp-17-3619-2017, 2017.

GRUAN: Access to RS92-GDP.2, GRUAN [data set], https://www.gruan.org/data/file-archive/rs92-gdp2-at-lc, last access: 1 March 2022.

Guan, H., Yau, M. K., and Davies, R.: The effects of longwave radiation in a small cumulus cloud, J. Atmos. Sci., 54, 2201–2214, https://doi.org/10.1175/1520-0469(1997)054<2201:TEOLRI>2.0.CO;2, 1997

Guo, J., Miao, Y., Zhang, Y., Liu, H., Li, Z., Zhang, W., He, J., Lou, M., Yan, Y., Bian, L., and Zhai, P.: The climatology of planetary boundary layer height in China derived from radiosonde and reanalysis data, Atmos. Chem. Phys., 16, 13309–13319, https://doi.org/10.5194/acp-16-13309-2016, 2016.

Guo, J., Liu, H., Li, Z., Rosenfeld, D., Jiang, M., Xu, W., Jiang, J. H., He, J., Chen, D., Min, M., and Zhai, P.: Aerosol-induced changes in the vertical structure of precipitation: a perspective of TRMM precipitation radar, Atmos. Chem. Phys., 18, 13329–13343, https://doi.org/10.5194/acp-18-13329-2018, 2018.

Guo, J. P., Li, Y., Cohen, J. B., Li, J., Chen, D. D., Xu, H., Liu, L., Yin, J. F., Hu, K. X., and Zhai, P. M.: Shift in the temporal trend of boundary layer height in China using long-term (1979–2016) radiosonde data, Geophys. Res. Lett., 46, 6080–6089, https://doi.org/10.1029/2019GL082666, 2019.

Guo, J., Zhang, J., Yang, K., Liao, H., Zhang, S., Huang, K., Lv, Y., Shao, J., Yu, T., Tong, B., Li, J., Su, T., Yim, S. H. L., Stoffelen, A., Zhai, P., and Xu, X.: Investigation of near-global daytime boundary layer height using high-resolution radiosondes: first results and comparison with ERA5, MERRA-2, JRA-55, and NCEP-2 reanalyses, Atmos. Chem. Phys., 21, 17079–17097, https://doi.org/10.5194/acp-21-17079-2021, 2021.

Hahn, C. J., Rossow, B., and Warren, S. G.: ISCCP cloud properties associated with standard cloud types identified in individual surface observations, J. Climate, 14, 11–28, https://doi.org/10.1175/1520-0442(2001)014<0011:ICPAWS>2.0.CO;2, 2001.

Hassim, M. E. E., Lane, T. P., and May, P. T.: Ground-based observations of overshooting convection during the Tropical Warm Pool-International Cloud Experiment, J. Geophys. Res.- Atmos., 119, 880–905, https://doi.org/10.1002/2013jd020673, 2014.

Hersbach, H., Bell, B., Berrisford, P., Hirahara, S., Horányi, A., Muñoz-Sabater, J., Nicolas, J., Peubey, C., Radu, R., Schepers, D., Simmons, A., Soci, C., Abdalla, S., Abellan, X., Balsamo, G., Bechtold, P., Biavati, G., Bidlot, J., Bonavita, M., De Chiara, G., Dahlgren, P., Dee, D., Diamantakis, M., Dragani, R., Flemming, J., Forbes, R., Fuentes, M., Geer, A., Haimberger, L., Healy, S., Hogan, R. J., Hólm, E., Janisková, M., Keeley, S., Laloyaux, P., Lopez, P., Lupu, C., Radnoti, G., de Rosnay, P., Rozum, I., Vamborg, F., Villaume, S., and Thépaut, J.- N.: The ERA5 global reanalysis, Q. J. Roy. Meteor. Soc., 146, 1999–2049, https://doi.org/10.1002/qj.3803, 2020.

Huang, H. Y. and Margulis, S. A.: Impact of soil moisture heterogeneity length scale and gradients on daytime coupled land-cloudy boundary layer interactions, Hydrol. Progress., 27, 1988–2003, https://doi.org/10.1002/hyp.9351, 2013.

Hollars, S., Fu, Q., Comstock, J., and Ackerman, T.: Comparison of cloud-top height retrievals from ground-based 35 GHz MMCR and GMS-5 satellite observations at ARM TWP Manus site, Atmos. Res., 72, 169–186, https://doi.org/10.1016/j.atmosres.2004.03.015, 2004.

Homeyer, C. R. and Kumjian, M. R.: Microphysical characteristics of overshooting convection from polarimetric radar observations, J. Atmos. Sci., 72, 870–891, https://doi.org/10.1175/jas-d-13-0388.1, 2015.

Houghton, J. T. Meira Filho, L. G., Callander, B. A., Harris, N., Kattenberg, A., and Maskell, K.: Climate change 1995: the science of climate change, Contribution of Working Group I to the Second Assessment Report of the Intergovernmental Panel on Climate Change, United Kingdom, https://www.ipcc.ch/report/ar2/wg1/ (last access: 8 February 2023), 1996.

Hyland, R. W. and Wexler, A.: Formulations for the thermodynamic properties of the saturated phases of H_2O from 173.15 K to 473.15 K, ASHRAE Tran., 89, 500–519, https://doi.org/10.1061/(ASCE)0733-9364(1984)110:4(533), 1983.

Immler, F., Treffeisen, R., Engelbart, D., Krüger, K., and Schrems, O.: Cirrus, contrails, and ice supersaturated regions in high pressure systems at northern mid latitudes, Atmos. Chem. Phys., 8, 1689–1699, https://doi.org/10.5194/acp-8-1689-2008, 2008.

IPCC: Summary for Policymakers, in: Climate Change 2021: The Physical Science Basis. Contribution of Working Group I to the Sixth Assessment Report of the Intergovernmental Panel on Climate Change, edited by: Masson-Delmotte, V., Zhai, P., Pirani, A., Connors, S. L., Péan, C., Berger, S., Caud, N., Chen, Y., Goldfarb, L., Gomis, M. I., Huang, M., Leitzell, K., Lonnoy, E., Matthews, J. B. R., Maycock, T. K., Waterfield, T., Yelekçi, O., Yu, R. and Zhou, B., Cambridge University Press, https://doi.org/10.1017/9781009157896, 2021.

Jauhiainen, H. and Lehmuskero, M.: Vaisala White Paper, Performance of the Vaisala radiosonde RS92-SGP and Vaisala DigiCORA sounding system MW31 in the WMO Mauritius radiosonde intercomparison, February, Vaisala, http://www.vaisala.com (last access: 12 June 2023), 2005.

Jensen, M. P., Holdridge, D. J., Survo, P., Lehtinen, R., Baxter, S., Toto, T., and Johnson, K. L.: Comparison of Vaisala radiosondes RS41 and RS92 at the ARM Southern Great Plains site, Atmos. Meas. Tech., 9, 3115–3129, https://doi.org/10.5194/amt-9-3115-2016, 2016.

Johnson, R. H., Rickenbach, T. M., Rutledge, S. A., Ciesielski, P. E., and Schubert, W. H.: Trimodal characteristics of tropical convection, J. Climate, 12, 2397–2418, https://doi.org/10.1175/1520-0442(1999)012<2397:TCOTC>2.0.CO;2, 1999.

Kato, S., Rose, F. G., Sun-Mack, S., Miller, W. F., Chen, Y., Rutan, D. A., Stephens, G. L., Loeb, N. G., Minnis, P., Wielicki, B. A., Winker, D. M., Charlock, T. P., Stackhouse, P. W., Xu, K. M., and Collins, W. D.: Improvements of top-of-atmosphere and surface irradiance computations with CALIPSO-, CloudSat-, and MODIS-derived cloud and aerosol properties, J. Geophys. Res., 116, D19209, https://https://doi.org/10.1029/2011JD016050, 2011.

Kim, S. W., Chung, E. S., Yoon, S. C., Sohn, B. J., and Sugimoto, N.: Intercomparisons of cloud-top and cloud-base heights from ground-based Lidar, CloudSat and CALIPSO measurements, Int. J. Remote Sens., 32, 1179–1197, https://doi.org/10.1080/01431160903527439, 2011.

Krämer, M., Schiller, C., Afchine, A., Bauer, R., Gensch, I., Mangold, A., Schlicht, S., Spelten, N., Sitnikov, N., Borrmann, S., de Reus, M., and Spichtinger, P.: Ice supersaturations and cirrus cloud crystal numbers, Atmos. Chem. Phys., 9, 3505–3522, https://doi.org/10.5194/acp-9-3505-2009, 2009.

Lawson, R. P. and Cooper, W. A.: Performance of some airborne thermometers in clouds, J. Atmos. Ocean. Tech., 7, 480–494, https://doi.org/10.1175/1520-0426(1990)007<0480:POSATI>2.0.CO;2, 1990.

Lawrence, M. G.: The relationship between relative humidity and the dewpoint temperature in moist air: A simple conversion and applications, B. Am. Meteorol. Soc., 8, 225–234, https://doi.org/10.1175/BAMS-86-2-225, 2005.

Lee, Y. J., Titov, D. V., Ignatiev, N. I., Tellmann, S., Patzold, M., and Piccioni, G.: The radiative forcing variability caused by the changes of the upper cloud vertical structure in the Venus mesosphere, Planet. Space Sci., 113, 298–308, https://doi.org/10.1016/j.pss.2014.12.006, 2015.

Loeb, N. G., Kato, S., Su, W. Y., Wong, T., Rose, F. G., Doelling, D. R., Norris, J. R., and Huang, X. L.: Advances in understanding top-of-atmosphere radiation variability from satellite observations, Surv. Geophys., 33, 359–385, https://doi.org/10.1007/s10712-012-9175-1, 2012.

Li, D., Liu, Y. Z., Shao, T. B., Luo, R., and Tan, Z. Y.: Assessment of cloud base height product from ERA5 reanalysis using ground-based observations, Chinese J. Atmos. Sci., in press, https://doi.org/10.3878/j.issn.1006-9895.2208.22109, 2022.

Li, F.: New Developments with Upper-air Sounding in China, Instruments and Observing Methods Report, No. 94, WMO/TD, No.1354, Geneva, WMO, https://library.wmo.int/idurl/4/35327 (last access: 9 June 2023), 2006.

Li, W., Xing, Y., and Ma, S.: The analysis and comparison between GTS1 radiosonde made in China and RS92 radiosonde of Vaisala company, Meteorological Monthly, 35, 97–102, 2009 (in Chinese).

Liu, C., Wang, T. J., Rosenfeld, D., Zhu, Y. N., Yue, Z. G., Yu, X., Xie, X. D., Li, S., Zhuang, B. L., Cheng, T. T., and Niu, S. J.: Anthropogenic effects on cloud condensation nuclei distribution and rain initiation in East China, Geophys. Res. Lett., 47, e2019GL086184, https://doi.org/10.1029/2019GL086184, 2020.

Liu, F. F., Zhu, B. Y., Lu, G. P., and Ma, M.: Outbreak of negative narrow bipolar events in two mid-latitude thunderstorms featuring overshooting tops, Remote. Sens., 13, 5130, https://doi.org/10.3390/rs13245130, 2021.

Liou, K. N.: Influence of cirrus clouds on weather and climate process: A global perspective, Mon. Weather Rev., 114, 1167–1199, https://doi.org/10.1175/1520-0493(1986)114<1167:IOCCOW>2.0.CO;2, 1986.

Luo, Y., Zhang, R., and Wang, H.: Comparing occurrences and vertical structures of hydrometeors between eastern China and the Indian monsoon region using CloudSat/CALIPSO data, J. Climate, 22, 1052–1064, https://doi.org/10.1175/2008jcli2606.1, 2009.

Mace, G. G. and Benson, S.: The vertical structure of cloud oc-currence and radiative forcing at the SGP ARM site as revealed by 8 years of continuous data, J. Climate, 21, 2591–2610, https://doi.org/10.1175/2007JCLI1987.1, 2008.

Mace, G. G., Ackerman, T. P., Minnis, P., and Young, D. F.: Cirrus layer microphysical properties derived from surface-based millimeter radar and infrared interferometer data, J. Geophys. Res., 103, 23207–23216, https://doi.org/10.1029/98JD02117, 1998.

Mao, X., Zhang, J., Xiao, S., Liu, Q., Chen, Y., Dai, W., and Yang, J.: Research on corrections of humidity measurements errors from GTS1 radiosonde based on fluid dynamic analysis, Chinese J. Geophys., 59, 4791–4805, https://doi.org/10.6038/cjg20161237, 2016 (in Chinese).

Marti, J. and Mauersberger, K.: A survey and new measurements of ice vapor pressure at temperatures between 170 and 250 K, Geophys. Res. Lett., 20, 363–366, https://doi.org/10.1029/93GL00105, 1993.

Martins, E., Noel, V., and Chepfer, H.: Properties of cirrus and subvisible cirrus from nighttime Cloud-Aerosol Lidar with Orthogonal Polarization (CALIOP), related to atmospheric dynamics and water vapor, J. Geophys. Res.-Atmos., 116, D02208, https://doi.org/10.1029/2010JD014519, 2011.

Matveev, L. T.: Chapter 7 Vertical structure of a cloud field in Clouds dynamics, Atmos. Ocean. Sci. Lib., 2, 198–230, https://doi.org/10.1007/978-94-009-6360-3, 1981.

Mauger, G. S. and Norris, J. R.: Assessing the impact of meteorological history on subtropical cloud fraction, J. Climate, 23, 2926–2940, https://doi.org/10.1175/2010JCLI3272.1, 2010.

Meehl, G. A. and Washington, W. M.: Cloud albedo feedback and the super greenhouse effect in a global coupled GCM, Clim. Dynam., 11, 399–411, https://doi.org/10.1007/BF00209514,1995.

Miao, H., Wang, X. C., Liu, Y. M., and Wu, G. X.: An evaluation of cloud vertical structure in three reanalyses against CloudSat/cloud-aerosol lidar and infrared pathfinder satellite observations, Atmos Sci. Lett., 20, e906, https://doi.org/10.1002/asl.906, 2019.

Miloshevich, L. M., Vomel, H., Whiteman, D. N., and Leblanc, T.: Accuracy assessment and correction of Vaisala RS92 radiosonde water vapor measurements, J. Geophys. Res., 114, D11305, https://doi.org/10.1029/2008JD011565, 2009.

Minnis, P., Yi, Y. H., Huang, J. P., and Ayers, K.: Relationships between radiosonde and RUC-2 meteorological conditions and cloud occurrence determined from ARM data, J. Geophys. Res., 110, D23204, https://doi.org/10.1029/2005JD006005, 2005.

Moran, K. P., Martner, B. E., Post, M. J., Kropfli, R. A., Welsh, D. C., and Widener, K. B.: An unattended cloud-profiling radar for use in climate research, B. Am. Meteorol. Soc., 79, 443–455, https://doi.org/10.1175/1520-0477(1998)079<0443:AUCPRF>2.0.CO;2, 1998.

Monteith, J. L. and Unsworth, M. H.: Principles of Environmental Physics, Third Ed. AP, Amsterdam, Elsevier Science, https://www.ebooks.com/en-us/book/631866/principles-of-environmental-physics/john-monteith/ (last access: 16 November 2022), 2008.

Muñoz Sabater, J.: ERA5-Land hourly data from 1950 to present, Copernicus Climate Change Service (C3S) Climate Data Store (CDS), https://doi.org/10.24381/cds.e2161bac, 2019.

Murphy, D. M. and Koop, T.: Review of the vapour pressures of ice and supercooled water for atmospheric applications, Q. J. Roy.

Meteor. Soc., 131, 1539–1565, https://doi.org/10.1256/qj.04.94, 2005.

Murray, F. W.: On the computation of saturation vapour pressure, J. Appl. Meteorol. Clim., 6, 203–204, https://doi.org/10.1175/1520-0450(1967)006<0203:OTCOSV>2.0.CO;2, 1967.

Nam, C., Bony, S., Dufresne, J. L., and Chepfer, H.: The 'too few, too bright' tropical low-cloud problem in CMIP5 models, Geohpys. Res. Lett., 39, L21801, https://doi.org/10.1029/2012GL053421, 2012.

Naud, C. M., Muller, J.-P., and Clothiaux, E. E.: Comparison between active sensor and radiosonde cloud boundaries over the ARM southern great plains site, J. Geophys. Res., 108, 4140, https://doi.org/10.1029/2002JD002887, 2003.

Naud, C. M., Muller, J.-P., Clothiaux, E. E., Baum, B. A., and Menzel, W. P.: Intercomparison of multiple years of MODIS, MISR and radar cloud-top heights, Ann. Geophys., 23, 2415–2424, https://doi.org/10.5194/angeo-23-2415-2005, 2005.

NOAA: Index of /data/us-radiosonde-bufr/archive, NOAA [data set], https://www.ncei.noaa.gov/data/us-radiosonde-bufr/archive/, last access: 1 March 2022.

Noel, V., Chepfer, H., Chiriaco, M., and Yorks, J.: The diurnal cycle of cloud profiles over land and ocean between 51° S and 51° N, seen by the CATS spaceborne lidar from the International Space Station, Atmos. Chem. Phys., 18, 9457–9473, https://doi.org/10.5194/acp-18-9457-2018, 2018.

Nowak, D., Ruffieux, D., Agnew, J. L., and Vuilleumier, L.: Detection of fog and low cloud boundaries with ground-based remote sensing systems, J. Atmos. Ocean. Tech., 25, 1357–1368, https://doi.org/10.1175/2007JTECHA950.1, 2008.

Oreopoulos, L., Cho, N., and Lee, D.: New insights about cloud vertical structure from CloudSat and CALIPSO observations, J. Geophys. Res.-Atmos., 122, 9280–9300, https://doi.org/10.1002/2017JD026629, 2017.

Pietrowicz, J. A. and Schiermeir, F. A.: Observational evidence of systematic radiosonde temperature sensing anomalies, J. Appl. Meteorol. Clim., 17, 1572–1575, https://doi.org/10.1175/1520-0450(1978)017<1572:OEOSRT>2.0.CO;2, 1978.

Platnick, S., King, M. D., Ackerman, S. A., Menzel, W. P., Baum, B. A., Riedi, J. C., and Frey, R. A.: The MODIS cloud products: Algorithms and examples from Terra, IEEE T. Geosci. Remote, 41, 459–473, https://doi.org/10.1109/TGRS.2002.808301, 2003.

Poore, K., Wang, J., and Rossow, W.: Cloud layer thicknesses from a combination of surface and upper-air observations, J. Climate, 8, 550–568, https://doi.org/10.1175/1520-0442(1995)008<0550:CLTFAC>2.0.CO;2, 1995.

Prein, A. F., Langhans, W., Fosser, G., Ferrone, A., Ban, N., Goergen, K., Keller, M., Tölle, M., Gutjahr, O., Feser, F., Brisson, E., Kollet, S., Schmidli, J., van Lipzig, N. P. M., and Leung, R.: A review on regional convection-permitting climate modeling: Demonstrations, prospects, and challenges, Rev. Geophys., 53, 323–361, https://https://doi.org/10.1002/2014RG000475, 2015.

Ramanathan, V., Cess, R. D., Harrison, E. F., Minnis, P., Barkstrom, B. R., Ahmad, E., and Hartmann, D.: Cloud-radiative forcing and climate: Results from the earth radiation budget experiment, Science, 243, 57–63, 1989.

Randall, D., Khairoutdinov, M., Arakawa, A., and Grabowski, W.: Breaking the cloud parameterization deadlock, B. Am. Meteo-

rol. Soc., 84, 1547–1564, https://doi.org/10.1175/BAMS-84-11-1547, 2003.

Narendra Reddy, N., Venkat Ratnam, M., Basha, G., and Ravikiran, V.: Cloud vertical structure over a tropical station obtained using long-term high-resolution radiosonde measurements, Atmos. Chem. Phys., 18, 11709–11727, https://doi.org/10.5194/acp-18-11709-2018, 2018.

Rogers, D. P., and Koračin, D.: Radiative transfer and turbulence in the cloud-topped marine atmospheric boundary layer, J. Atmos. Sci., 49, 1473–1486 https://doi.org/10.1175/1520-0469(1992)049<1473:RTATIT>2.0.CO;2, 1992.

Rosenfeld, D., Fromm, M., Trentmann, J., Luderer, G., Andreae, M. O., and Servranckx, R.: The Chisholm firestorm: observed microstructure, precipitation and lightning activity of a pyro-cumulonimbus, Atmos. Chem. Phys., 7, 645–659, https://doi.org/10.5194/acp-7-645-2007, 2007.

Schoeberl, M. R., Wang, Y., Ueyama, R., Taha, G., Jensen, E., and Yu, W.: Analysis and impact of the Hunga Tonga-Hunga Ha'apai stratospheric water vapor plume, Geophys. Res. Lett., 49, e2022GL100248, https://doi.org/10.1029/2022GL100248, 2022

Shan, P., Mao, X., Zhang, J., Ma, T., and Chen, Y.: Correction of solar radiation dry bias of radiosonde humidity based on PSO-BP neural network, Science Technology and Engineering, 18, 1–8, 2018 (in Chinese).

Sharma, S., Dass, A., Mishra, A. K., Singh, S., and Kumar, K.: A decadal climatology cloud vertical structure over the Indo-Gangetic Plain using radiosonde and radar observations, Atmos. Res., 266, 105949, https://doi.org/10.1016/j.atmosres.2021.105949, 2022.

Solomon, S. D., Qin, D., Manning, M., Chen, Z., Marquis, M., Avery, K. B., Tignor, M., and Miller, H. L.: Climate Change 2007: The Physical Science Basis: Contribution of Working Group I to the Fourth Assessment Report of the Intergovernmental Panel on Climate Change, Cambridge University Press, Cambridge, UK and New York, NY, USA, 996, http://www.ipcc.ch/ipccreports/ar4/wg1 (last access: 12 January 2023), 2007.

Sonntag, D.: Important new values of the physical constants of 1986, vapour pressure formulations based on the ITS-90, and psychrometer formulae, Z. Meteorol., 40, 340–344, 1990.

Stephens, G. L.: Cloud feedbacks in the climate system: A critical review, J. Climate, 18, 237–273, https://doi.org/10.1175/JCLI-3243.1, 2005.

Stephens, G. L., Vane, D. G., Boain, R. J., Mace, G. G., Sassen, K., Wang, Z., Illingworth, A., O'Connor, E., Rossow, W. B., Durden, S. L., Miller, S. D., Austin, R. T., Benedetti, A., and Mitrescu, C.: The CloudSat Science Team: The CloudSat mission and the A-Train: a new dimension of space-based observation of clouds and precipitation, B. Am. Meteorol. Soc., 83, 1771–1790, https://doi.org/10.1175/BAMS-83-12-1771, 2002.

Stephens, G. L., Li, J. L., Wild, M., Clayson, C. A., Leob, N., Kato, S., L'Ecuyer, T., Stackhouse, P. W., Lebsock, M., and Andrews, T.: An update on Earth's energy balance in light of the latest global observations, Nat. Geosci., 5, 691–696, https://doi.org/10.1038/NGEO1580, 2012.

Stokes, G. M. and Schwartz, S. E.: The atmospheric radiation measurement (ARM) program: Programmatic background and design of the cloud and radiation test bed, B. Am. Meteorol. Soc., 75, 1202–1221, https://doi.org/10.1175/1520-0477(1994)075<1201:TARMPP>2.0.CO;2, 1994.

Stubenrauch, C. J., Rossow, W. B., Kinne, S., Ackerman, S., Cesana, G., Chepfer, H., Di Girolamo, L., Getzewich, B., Guignard, A., Heidinger, A., Maddux, B. C., Menzel, W. P., Minnis, P., Pearl, C., Platnick, S., Poulsen, C., Riedi, J., Sun-Mack, S., Walther, A., Winker, D., Zeng, S., and Zhao, G.: Assessment of global cloud datasets from satellites: Project and database initiated by the GEWEX radiation panel, B. Am. Meteorol. Soc., 94, 1031–1049, https://doi.org/10.1175/BAMS-D-12-00117.1, 2013.

Subrahmanyam, K. V. and Kumar, K. K.: CloudSat observations of multi layered clouds across the globe, Clim. Dynam., 49, 327–341, https://doi.org/10.1007/s00382-016-3345-7, 2017.

Sugimoto, N., Matsui, I., Shimizu, A., Pinandito, M., and Sugondo, S.: Climatological characteristics of cloud distribution and planetary boundary layer structure in Jakarta, Indonesia revealed by lidar observation, Geophys. Res. Lett., 27, 2909–2912, https://doi.org/10.1029/2000GL011544, 2000.

Sun, G. H., Hu, Z. Y., Ma, Y. M., Xie, Z. P., Yang, S., and Wang, J. M.: Analysis of local land-atmosphere coupling in rainy season over a typical underlying surface in Tibetan Plateau based on field measurements and ERA5, Atmos. Res., 243, 105025, https://doi.org/10.1016/j.atmosres.2020.105025, 2020.

Sun, G. R., Li, Y. Y., and Liu, L. H.: Why is there a titled cloud vertical structure associated with the northward advance of the East Asian summer monsoon, Atmos. Sci. Lett., 20, e903, https://doi.org/10.1002/asl.903, 2019.

Trenberth, K. E., Fasullo, J. T., and Kiehl, J.: Earth's global energy budget, B. Am. Meteorol. Soc., 90, 311–323, https://doi.org/10.1175/2008BAMS2634.1, 2009.

Vaisala: Vaisala Radiosonde RS41-SGP. Ref. B211444EN-E © Vaisala, https://www.vaisala.com/sites/default/files/documents/WEA-MET-RS41SGP-Datasheet-B211444EN.pdf (last access: 26 July 2023), 2017.

Viúdez-Mora, A., Costa-Surós, M., Calbó, J., and Gonzalez, J. A.: Modeling atmospheric longwave radiation at the surface during overcast skies: The role of cloud base height, J. Geophys. Res.-Atmos., 120, 199–214, https://https://doi.org/10.1002/2014JD022310, 2015.

Vogelezang, D. H. P. and Holtslag, A. A. M.: Evaluation and model impacts of alternative boundary-layer height formulation, Bound.-Lay. Meteorol., 81, 245–269, https://doi.org/10.1007/BF02430331, 1996.

Vömel, H., Selkirk, H., Miloshevich, L., Valverde-Canossa, J., Valdes, J., Kyro, E., Kivi, R., Stolz, W., Peng, G., and Diaz, J. A.: Radiation dry bias of the Vaisala RS92 humidity sensor, J. Atmos. Ocean. Tech., 24, 953–963, https://doi.org/10.1175/JTECH2019.1, 2007.

Wall, C., Zipser, E., and Liu, C. T.: An investigation of the aerosol indirect effect on convective intensity using satellite observations, J. Atmos. Sci., 71, 430–447, https://doi.org/10.1175/JAS-D-13-0158.1, 2014.

Wang, J. and Rossow, W.: Determination of cloud vertical structure from upper-Air observations, J. Appl. Meteorol., 34, 2243–2258, https://doi.org/10.1175/1520-0450(1995)034<2243:DOCVSF>2.0.CO;2, 1995.

Wang, J., Rossow, W. B., and Zhang, Y. C.: Cloud vertical structure and its variations from a 20-yr global rawinsonde dataset, J. Climate, 13, 3041–3056, https://doi.org/10.1175/1520-0442(2000)013<3041:CVSAIV>2.0.CO;2, 2000.

Wang, J. H., Zhang, L. Y., Dai, A. G., Immler, F., Sommer, M., and Vömel, H.: Radiation dry bias correction of Vaisala RS92 humidity data and its impacts on historical radiosonde data, J. Atmos. Ocean. Tech., 30, 197–214, https://doi.org/10.1175/JTECH-D-12-00113.1, 2013.

Wang, R. J., Zhou, R. J., Yang, S. P., Li, R., Pu, I. P., Liu, K. Y., and Deng, Y.: A new algorithm for estimating low cloud-base height in southwest China, J. Appl. Meteorol. Clim., 61, 1179–1197, https://doi.org/10.1175/JAMC-D-21-0221.1, 2022.

Wang, Y. J., Xu, X. D., Zhao, Y., and Wang, M. Z.: Variation characteristics of the planetary boundary layer height and its relationship with $PM_{2.5}$ concentration over China, J. Trop. Meteorol., 24, 385–394, https://doi.org/10.16555/j.1006-8775.2018.03.011, 2018.

Waliser, D. E., Li, J-L. F., Woods, C. P., Austin, R. T., Bacmeister, J., Chern, J., Genio, A. D., Jiang, J. H., Kuang, Z., Meng, H., Minnis, P., Platnick, S., Rossow, W. B., Stephens, G. L., Sun-Mack, S, Tao, W.-K. Tompkins, A. M., Vane, D. G., Walker, C., and Wu, D.: Cloud ice: A climate model challenge with signs and expectations of progress, J. Geophys. Res., 114, D00A21, https://doi.org/10.1029/2008JD010015, 2009.

Weare, B. C.: Insights into the importance of cloud vertical structure in climate, Geophys. Res. Lett., 27, 907–910, https://doi.org/10.1029/1999GL011214, 2000.

Wei, J. F., Zhao, J. W., Chen, H. S., and Liang, X. Z.: Coupling between land surface fluxes and lifting condensation level: mechanisms and sensitivity to model physics parameterizations, J. Geophys. Res.-Atmos., 126, e2020JD034313, https://doi.org/10.1029/2020JD034313, 2021.

Wielicki, B. A., Cess, R. D., King, M. D., Randall, D. A., and Harrison, E. F.: Mission to planet Earth: Role of clouds and radiation in climate, B. Am. Meteorol. Soc., 76, 2125–2154, https://doi.org/10.1038/NGEO1580, 1995.

Willen, U., Crewell, S., Baltink, H. K., and Sievers, O.: Assessing model predicted vertical cloud structure and cloud overlap with radar and lidar ceilometer observations for the Baltex Brige Campagin of CLIWA-NET, Atmos. Res., 75, 227–255, https://doi.org/10.1016/j.atmosres.2004.12.008, 2005.

Wild, M.: New Directions: A facelift for the picture of the global energy balance, Atmos. Environ., 55, 366–367, https://doi.org/10.1016/j.atmosenv.2012.03.022, 2012.

Winker, D. M., Hunt, W. H., and McGill, M. J.: Initial performance assessment of CALIOP, Geophys. Res. Lett., 34, L19803, https://doi.org/10.1029/2007GL030135, 2007.

Winker, D. M., Vaughan, M. A., Omar, A., Hu, Y., Powell, K. A., Liu, Z., Hunt, W. H., and Young, S. A.: Overview of the CALIPSO mission and CALIOP data processing algorithms, J. Atmos. Ocean. Tech., 26, 2310–2323, https://doi.org/10.1175/2009JTECHA1281.1, 2009.

WMO: Meteorology – A three-dimensional science: Second session of the commission for aerology, WMO Bull., 4, 134–138, 1957.

Xi, B. X., Dong, X. Q., Minnis, P., and Khaiyer, M. M.: A 10-year climatology of cloud fraction and vertical distribution derived from both surface and GOES observations over the DOE ARM SGP site, J. Geophys. Res.-Atmos., 115, D12124, https://doi.org/10.1029/2009JD012800, 2010.

Xu, G. R., Zhang, W. G., Wan, X., and Wang, B.: Cloud occurrence frequency and cloud liquid water path for non-precipitating clouds using ground-based measurements over central China, J. Atmos. Sol.-Terr. Phy., 215, 105575, https://doi.org/10.1016/j.jastp.2021.105575, 2021a.

Xu, H., Guo, J. P., Li, J., Liu, L., Chen, T. M., Guo, X. R., Lyu, Y. M., Wang, D., Han, Y., Chen, Q., and Zhang, Y.: The Significant Role of Radiosonde-measured Cloud-base Height in the Estimation of Cloud Radiative Forcing, Adv. Atmos. Sci., 38, 1552–1565, https://doi.org/10.1007/s00376-021-0431-5, 2021b.

Yoneyama, K., Fujita, M., Sato, N., Fujiwara, M., Inai, Y., and Hasebe, F.: Correction for radiation dry bias found in RS92 radiosonde data during the MISMO field experiment, SOLA, 4, 13–16, https://doi.org/10.2151/sola.2008-004, 2008.

Zhang, D., Wang, Z., Luo, T., Yin, Y., and Flynn, C.: The occurrence of ice production in slightly supercooled Arctic stratiform clouds as observed by ground-based remote sensors at the ARM NSA site, J. Geophys. Res.-Atmos., 122, 2867–2877, https://doi.org/10.1002/2016JD026226, 2017.

Zhang, J. Q, Chen, H. B., Li, Z. Q., Fan, X. H., Peng, L. A., Yu, Y., and Cribb, M.: Analysis of cloud layer structure in Shouxian, China using RS92 radiosonde aided by 95 GHz cloud radar, J. Geophys. Res.-Atmos., 115, D00K30, https://doi.org/10.1029/2010JD014030, 2010.

Zhang, J. Q., Chen, H. B., Bian, J. C., Xuan, Y. J., Duan, Y. J., and Cribb, M.: Development of cloud detection methods using CFH, GTS1, and RS80 radiosondes, Adv. Atmos. Sci., 29, 236–248, https://doi.org/10.1007/s00376-011-0215-4, 2012.

Zhang, J. Q., Li, Z. Q., Chen, H. B., Yoo, H., and Cribb, M.: Cloud vertical distribution from radiosonde, remote sensing, and model simulations, Clim. Dynam., 43, 1129–1140, https://doi.org/10.1007/s00382-014-2142-4, 2014.

Zhang, Y., Zhang, L. J., Guo, J. P., Feng, J. M., Cao, L. J., Wang, Y., Zhou, Q., Li, L. X., Li, B., Xu, H., Liu, L., An, N., and Liu, H.: Climatology of cloud-base height from long-term radiosonde measurements in China, Adv. Atmos. Sci., 35, 158–168, https://doi.org/10.1007/s00376-017-7096-0, 2018.

Zhang, Y., Zhou, Q., Lv, S., Jia, S., Tao, F., Chen, D., and Guo, J.: Elucidating cloud vertical structures based on three-year Ka-band cloud radar observations from Beijing, China, Atmos. Res., 222, 88–99, https://doi.org/10.1016/j.atmosres.2019.02.007, 2019.

Zhang, Y. Y. and Klein, S.: Factors controlling the vertical extent of fair-weather shallow cumulus clouds over land: investigation of diurnal-cycle observations collected at the ARM southern great plains site, J. Atmos. Sci., 70, 1297–1315, https://doi.org/10.1175/JAS-D-12-0131.1, 2013.

Zhou, Q., Zhang, Y., Jia, S. Z., Jin, J. L., Lv, S. S., and Li, Y. N.: Climatology of cloud vertical structures from long-term high-resolution radiosonde measurements in Beijing, Atmosphere, 11, 401, https://doi.org/10.3390/atmos11040401, 2020.

Zhou, R., Wang, G., and Zhaxi, S. L.: Cloud vertical structure measurements from a ground-based cloud radar over the southeastern Tibetan Plateau, Atmos. Res., 258, 105629, https://doi.org/10.1016/j.atmosres.2021.105629, 2021.